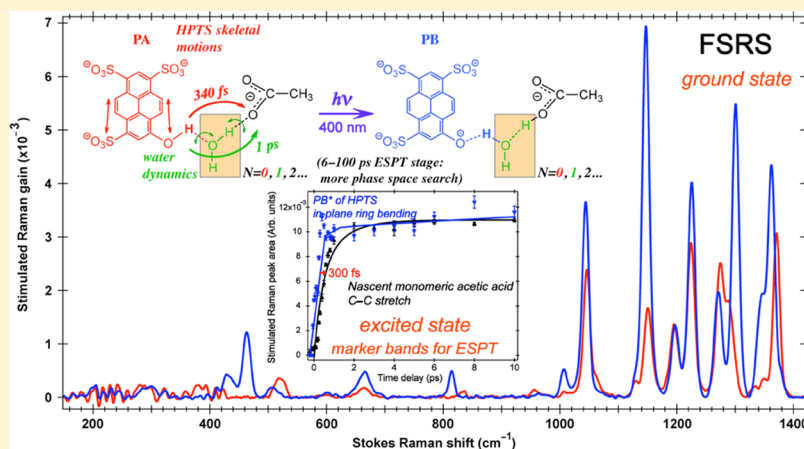


Ultrafast Conformational Dynamics of Pyranine during Excited State Proton Transfer in Aqueous Solution Revealed by Femtosecond Stimulated Raman Spectroscopy

Weimin Liu, Fangyuan Han, Connor Smith, and Chong Fang*

Department of Chemistry, Oregon State University, Corvallis, Oregon 97331, United States

S Supporting Information



ABSTRACT: Proton transfer reaction plays an essential role in a myriad of chemical and biological processes, and to reveal the choreography of the proton motion intra- and intermolecularly, a spectroscopic technique capable of capturing molecular structural snapshots on the intrinsic time scale of proton transfer motions is needed. The photoacid pyranine (8-hydroxypyrene-1,3,6-trisulfonic acid, HPTS) serves as a paradigm case to dissect excited state proton transfer (ESPT) events in aqueous solution, triggered precisely by photoexcitation. We have used femtosecond stimulated Raman spectroscopy (FSRS) to yield novel insights into the ultrafast conformational dynamics of photoexcited HPTS in complex with water and acetate molecules. Marker bands attributed to the deprotonated form of HPTS (1139 cm^{-1} , $\sim 220\text{ fs}$ rise) appear earlier and faster than the monomer acetic acid peak (864 cm^{-1} , $\sim 530\text{ fs}$ rise), indicating that water molecules actively participate in the ESPT chain. Several key low-frequency modes at 106 , 150 , 195 , and 321 cm^{-1} have been identified to facilitate ESPT at different stages from 300 fs , 1 ps , to 6 ps and beyond, having distinctive dynamics contributing through hydrogen bonds with 0 , 1 , and more intervening water molecules. The time-resolved FSRs spectroscopy renders a direct approach to observe the reactive coupling between the vibrational degrees of freedom of photoexcited HPTS in action, therefore revealing the anharmonicity matrix both within HPTS and between HPTS and the neighboring acceptor molecules. The observed excited state conformational dynamics are along the ESPT multidimensional reaction coordinate and are responsible for the photoacidity of HPTS in aqueous solution.

I. INTRODUCTION

It is of fundamental interest to track molecular motions during a chemical reaction, but the main hurdle in obtaining that level of information is the detection resolution in the spatial and temporal domain. Among all chemical reactions, proton transfer in aqueous environments^{1,2} has been widely studied because they are ubiquitous for a multitude of biological functions such as enzymatic catalysis,³ proton pump and ion channel,⁴ bioluminescence,^{5–7} and photosynthesis.^{8,9} An effective experimental approach to study proton transfer is to investigate the proton release process of photoacids. The acidity of these photosensitive molecules can be changed by optical excitation, which makes it possible to precisely initiate proton transfer and monitor it as a function of time. Pyranine

(8-hydroxypyrene-1,3,6-trisulfonic acid, or HPTS) is a commonly used photoacid that possesses the intriguing property of dropping its pK_a value for almost 7 units upon electronic excitation, and serves as a pragmatic system to scrutinize the reaction mechanism for a photosensitive molecule undergoing excited state proton transfer (ESPT).

The ultrafast dynamics of HPTS have been the subject of numerous studies in aqueous solution by time-resolved

Special Issue: Richard A. Mathies Festschrift

Received: March 2, 2012

Revised: May 31, 2012

Published: June 6, 2012



electronic and vibrational spectroscopy. The optical excitation of the trigger pulse induces a transition from the electronic ground state (S_0) to a higher lying electronic excited state (typically S_1) of HPTS, with the subsequent ESPT followed by fluorescence emission and electronic absorption changes. These changes can be directly measured through time-resolved fluorescence emission¹⁰ and transient absorption spectroscopy^{11–13} using a probe pulse at the electronic resonance of HPTS in visible regions. However, these techniques do not directly detect the departure of a proton at the donor site or the arrival of a proton at the acceptor site, which lies in the fact that the fluctuations caused by solvent reorganization, energy dissipation (vibrational cooling), the transient electronic band of absorption or stimulated emission, and so on may overlap during ESPT.^{7,14} Recently, ESPT of HPTS–acetate (and chloroacetate) complexes in aqueous solution was studied using femtosecond UV-pump mid-infrared (IR)-probe spectroscopy,^{15–19} wherein the proton transfer processes were tracked by probing the vibrational marker modes of the HPTS photoacid form (e.g., IR-active aromatic ring C–O stretching modes at 1250–1600 cm^{-1}), the proton-accepting carboxylate base (C=O stretching mode of acetic acid at $\sim 1700 \text{ cm}^{-1}$), and the reaction intermediate (IR-active region between the stretching and bending region of $\text{H}_2\text{O}/\text{D}_2\text{O}$ at 2570/1850 cm^{-1} , respectively). Experimental results reveal distinct base-concentration-dependent proton transfer dynamics, and a distribution of hydrogen (H)-bonded reaction complexes with different numbers (mostly 1–5) of water molecules separating the acid and base are proposed to play an important role in ESPT.¹⁸ The results reported by the Nibbering group^{15–17} show three distinctive proton/deuteron transfer (PT/DT) pathways. The ultrafast component was attributed to PT/DT in preexisting H-bonded HPTS–acetate “tight” complexes in S_0 with a time constant of <150 femtoseconds (fs). The second transfer with a time constant of 6 to several tens of picoseconds (ps) was assigned to PT/DT in solvent-separated HPTS–acetate “loose” complexes. The slowest component has a time constant of tens of picoseconds to nanoseconds (ns) owing to the diffusive formation of tight and solvent-separated loose complexes. However, the skeletal motions and configurational rearrangement that are of particular importance in the processes of excited state intramolecular^{20–27} and/or intermolecular proton transfer^{5,7,28–31} (ESIPT and/or ESPT) following photoexcitation remain elusive, primarily because the corresponding vibrational frequency range of 100–500 cm^{-1} cannot be directly observed in the mid-IR region in water. Hitherto, the low-frequency modes during ESIPT have been extensively studied by resonance Raman spectroscopy,^{20,22,25} ultrafast pump–probe spectroscopy,^{21,23,24} and simulations.^{26,27,32} The molecular skeleton motions therein reduce the distance between the proton donor and acceptor that may reflect the largely different electronic character between the ground and excited electronic states and result in lowering the effective barrier to proton hopping.^{20,21,24,25} Recently, Fang and Mathies⁷ studied ESPT in the wild-type green fluorescent protein (wtGFP) using femtosecond stimulated Raman spectroscopy (FSRS),^{33–35} and obtained sufficiently detailed time-resolved vibrational spectra of the wtGFP chromophore reporting on its ultrafast excited state structural dynamics. The high-frequency vibrational modes were found to display frequency oscillation with a period of ~ 280 fs, which indicates skeletal motions (i.e., a 120 cm^{-1} two-ring wagging mode) are activated and strongly involved in ESPT, efficiently producing

the fluorescent form of the protein on the picosecond time scale.

The central aim of this work is to establish an effective approach to study ESPT in aqueous solution in the context of multidimensional reaction coordinate. What remains unclear from the literature are the exact low-frequency modes involved in the early stage of ESPT that *precedes* or *accompanies* the actual proton transfer, and the time scales involved with those easily accessible collective skeletal motions that are promptly activated by photoexcitation. As the molecule enters the reaction phase starting from the Franck–Condon (FC) region, various vibrational bands will be activated concomitantly or sequentially, which should be exposed by the time-resolved wavelength-dispersed spectroscopy such as FSRS. This information is critical in deciphering intra- and intermolecular energy transfer leading to free induction decay, and multidimensional reaction coordinate leading to chemical reactivity.

In this paper, we use FSRS to obtain the time-resolved excited-state Raman spectra of HPTS as it pushes the hydroxyl proton toward the acceptor, i.e., the acetate ion in water, on the femtosecond to picosecond time scale in the vibrational frequency range of 100–1450 cm^{-1} . This experiment enables the real-time tracking of the intermolecular ESPT along its trajectory from the initial bound state near the HPTS donor to its eventual position on the acetate acceptor. FSRS is a novel spectroscopic technique that allows a rapid acquisition of Raman spectra with simultaneously high temporal (<30 fs) and spectral (<10 cm^{-1}) resolution, and has been successfully used to inspect excited-state vibrational dynamics in a wide variety of photochemical and photobiological reaction systems.^{7,36–40} Starting from the electronic ground state Raman spectral analysis, we find significant difference of the photoacid (PA) and photobase (PB) form of HPTS with the acetate concentration change or pH change in water solution, which correlates nicely with their ultraviolet/visible (UV/Vis) spectra. The time-resolved FSRS measurement on 11 mM HPTS with 2 M acetate in water reveals a rich array of high- and low-frequency modes that show *distinctive* dynamics on the time scale of ESPT from time zero up to 150 ps, indicating that the reaction coordinate for ESPT of HPTS in acetate water is indeed multidimensional in nature. The characteristic skeletal motions associated with those key low-frequency modes are discussed with the aid of density functional theory (DFT) calculation.⁴¹ These nuclear motions sequentially contribute to the various stages of intermolecular ESPT in aqueous solution through the $\text{HPTS}\cdots(\text{H}_2\text{O})_n\cdots\text{acetate}$ [$n = 0, 1, \dots$] H-bonding chain.

II. EXPERIMENTAL METHODS

The photoacid pyranine (HPTS) was purchased from Aldrich ($\geq 97\%$) and TCI America ($\geq 85\%$), and the methoxy derivative of HPTS (8-methoxypyrene-1,3,6-trisulfonic acid trisodium salt, MPTS) was purchased from Anaspec. They were used without further purification. Acetic acid (CH_3COOH) and sodium acetate (CH_3COONa) were purchased from Mallinckrodt. The Raman spectra of intermolecular proton transfer reaction between the photoacid HPTS (11 mM) and sodium acetate with different concentrations of 0, 0.1, 0.5, 1, 2, and 3 M were studied in Millipore water solution after 0.22- μm filtration. The PB form of HPTS is prepared by dissolving 11 mM HPTS in sodium hydroxide (NaOH) water solution (pH = 12), and for comparison, the PA form of HPTS of the same concentration is made in water (pH = 6). A buffer solution

consisting of 2 M sodium acetate (NaAc) and 1.26 M acetic acid (HAc) was also prepared to maintain pH = 5.5. In this condition, HPTS is predominantly protonated (discussed later). HPTS and MPTS (20 mM) were both dissolved in this buffer solution for spectral measurement and comparison. No significant spectral differences are seen using samples prepared from 97% or 85% HPTS.

FSRS^{33,34} is performed using a newly built femtosecond laser system consisting of a mode-locked Ti:Sapphire oscillator (Mantis-5, Coherent) and regenerative amplifier (Legend Elite-USP-1K-HE, Coherent) which provides ~35 fs pulse centered at ~800 nm with mJ per pulse energies (average power ~4.1 W) at 1 kHz repetition rate. Half of the output energy is set aside for other spectroscopic experiments. The output laser beam of ~2 W is split into three beams to generate a narrow-bandwidth picosecond Raman pump pulse, a broadband femtosecond Raman probe pulse and a femtosecond actinic pulse mainly following previously published optical setups.^{7,33,34} In short, around 200 μ J/pulse of the laser amplifier output is collimated by a telescope lens system ($f = 150$, 50 mm) to decrease the beam size to ~3 mm and then frequency-doubled using a β -barium borate (BBO) crystal (type-I, phase matching angle $\theta = 27.8^\circ$, 0.3 mm thickness) to generate the actinic pump pulse at 400 nm with the pulse energy of 50 μ J/pulse. This photoexcitation pulse is rotated 90° by a $\lambda/2$ waveplate and then compressed by a prism pair (Suprasil-1, CVI Melles Griot) to ~40 fs, which is diagnosed using a 0.1 mm BK7 glass plate in a home-built third-order intensity autocorrelator based on polarization gating techniques. The pulse energy of the compressed actinic pump beam is ~10 μ J/pulse and varied by a circular variable neutral-density filter (OD = 0.05–2, Newport). The pulse polarization can be rotated by a $\lambda/2$ waveplate for various experimental purposes (optical Kerr effect (OKE) or FSRS).

About 15 μ J/pulse of the amplified output is focused using a $f = 100$ mm BK7 lens on a Z-cut single crystal sapphire plate with 2 mm thickness to generate supercontinuum white light, and then recollimated afterward by a $f = 50$ mm BK7 lens to a beam size of 2 mm (IR part of the continuum white light). The wavelength range from 810–910 nm of the white light that corresponds to ~150–1500 cm^{-1} Stokes Raman shift to the 800 nm fundamental is selected using a long-pass filter (color glass filter with cut-on 830 nm, RG830, Newport) and compressed with a fused silica prism pair to produce ~35 fs broadband Raman probe pulse. The pulse duration of Raman probe is measured with a type-I BBO ($\theta = 27.8^\circ$, 0.1 mm thickness) crystal by a homemade speaker-driven moving-mirror autocorrelator. The audio speaker is driven by a sine wave from a function generator (Sweep function generator, Heath 1274). To increase the signal-to-noise ratio (SNR) of the very weak second harmonic generation (SFG) autocorrelation signal, a lock-in amplifier (EG&G 5207) is used and synchronized with the laser repetition rate at 1 kHz. The autocorrelation signal is monitored by a digital oscilloscope (Tektronix TDS 2024c) triggered by the same function generator. The Raman pump pulse is produced by a homemade grating-based spectral filter.³³ About 1.2 W of the laser fundamental pulse is dispersed by a gold reflective grating (1200 grooves/mm, wavelength first order at 750 nm, blaze angle $\theta = 26.7^\circ$) and focused onto an adjustable slit by an $f = 150$ mm cylindrical lens. After the slit, a close-set mirror reflects back the spatially filtered pulse along the input path. The bandwidth compressed laser pulse is recollimated by the

cylindrical lens and grating and then picked off by a mirror. The slit width is set as 0.1 mm corresponding to the bandwidth of Raman pump ~10 cm^{-1} and pulse duration of 3.2 ps, which is measured by OKE of the cross correlation of Raman pump with the compressed actinic pulse at the sample position. The Raman pump is ~4 mW average power at the sample spot.

The actinic pump, Raman pump, and probe beams are set up in a crossing geometry that minimizes scattering background and interference effects caused by the Raman pump, as well as improves the SNR at the low-frequency region of the spectrum ($<400 \text{ cm}^{-1}$). All three beams are focused onto the sample cell by a parabolic reflective mirror instead of a lens to reduce pulse broadening and chirp. After the sample, a beam blocker is used to spatially block the Raman pump and actinic pump beams, while the Raman probe is recollimated by an $f = 100$ mm BK7 lens and focused into the spectrograph by a $f = 150$ mm BK7 lens. A long-pass filter (RG830) and a circular variable neutral-density filter (OD=0.05–1, Newport) are put in front of the spectrograph to further block the Raman pump scattering and avoid the signal saturation on the detector. Inside the spectrograph, the probe beam is dispersed by a 600 grooves/mm grating (wavelength first order at 1000 nm, blaze angle $\theta = 17.5^\circ$) and imaged on a front-illuminated charge-coupled device (CCD) camera (Princeton Instruments, PIXIS 100F) consisting of a 1340×100 pixel array.

The spatial overlap of the three beams is first achieved using a pinhole with 50 μ m diameter at the focal point of the parabolic reflect mirror. For prime temporal overlap, by using a type-I BBO crystal ($\theta = 27.8^\circ$, 0.3 mm thickness), the SFG signals generated by the Raman pump plus Raman probe as well as Raman probe plus actinic pump beams can be directly observed on a paper screen through adjusting the retroreflective delay lines in the Raman pump beam or actinic pump beam.

All the stimulated Raman spectra are calibrated using carbon tetrachloride (CCl_4) and ethanol ($\text{CH}_3\text{CH}_2\text{OH}$) mixed solution as a standard that spans the Raman frequency modes from ~200–1400 cm^{-1} . The ground state Raman signal of the standard is maximized through spatial overlap adjustment using a fine-tuning mirror mount in the Raman pump right before the parabolic mirror, and temporal overlap optimization using the micrometer-driven retroreflective delay line of the Raman pump. Each Raman gain spectrum is acquired through averaging and processing 3000 raw spectra (1500 spectra each with Raman pump on and off) and therefore 3 s acquisition time of one data set. To increase the SNR of the ground state signal, we normally collect 80 sets for one sample run. For the excited state FSRS spectra, the Raman pump and probe beams remain fixed at zero-time overlap, while the actinic pump is delayed by a computer-controlled stepper-motor-driven translation stage (07EAS504 with 17BSC101 controller, CVI Melles Griot). The spatial and temporal overlap of the actinic pump and Raman probe beams are finely adjusted using OKE of the sample solution before each excited state FSRS data collection. A representative plot of the frequency-resolved OKE signal is shown in Supporting Information Figure S1, with the instrument cross-correlation time of ~90 fs measured from a 0.1-mm-thick BK7 glass plate, and ~120 fs with the quartz sample cell.

A phase-locked optical chopper (New Focus 3501), which is synchronized with the laser output at 1 kHz, is used to chop the Raman pump beam at 500 Hz. The stimulated Raman spectrum is calculated from the expression $[(\text{Raman probe spectrum})_{\text{Raman pump on}}/(\text{Raman probe spectrum})_{\text{Raman pump off}}]$,

and displayed on-screen after averaging by a LabVIEW program incorporating STIK scientific imaging toolkit (R-Cubed software) for the CCD camera. The Raman probe intensity pulse-to-pulse fluctuations is $\sim 0.5\%$. In the actinic pump beam, an electronic shutter (LS6S2, with the single-channel shutter driver/timer VMM-T1, Uniblitz) is used to control the actinic pulse on/off at different time delays. The excited state FSRS spectrum at each delay point is obtained by the different spectrum of $[(\text{Raman gain spectrum})_{\text{actinic pump on}} - (\text{Raman gain spectrum})_{\text{actinic pump off}}]$ through collecting and averaging 10–20 sets of the different spectrum, with the total acquisition time at each time point of 30–60 s (15 000–30 000 averages per point). To reduce the thermal heating effect caused by the high peak power femtosecond-pulsed laser on the sample, the sample solution is contained in a short-path length (thickness = 1 mm) flow cell sandwiched by two 1-mm-thick quartz glass windows (48-Q-1, Starna Cells) and recirculated with a peristaltic pump (HP 89052B) with adjustable rate. All the data processing was done using Igor Pro (Version 6.22A, WaveMetrics, Inc.).

III. RESULTS

In order to reveal the fundamental yet complex excited state structural dynamics of HPTS molecules in aqueous solution, we have carried out a range of spectroscopic measurements and computations to pinpoint the characteristic vibrational bands responsible for the photoacidity of HPTS.

A. UV/Vis Spectroscopy of HPTS. HPTS is a highly fluorescent molecule, so it hinders conventional Raman measurement. The protonated form (PA) strongly absorbs at ~ 400 nm (see Figure 1) and transfers its proton to base acceptors, which could be the H-bonded water molecules if there is no stronger base present in solution. The green fluorescence emitted is due to the deprotonated form (PB) of HPTS that has a S_1 state (PB*) that lies lower in energy than the S_1 state of the protonated form (PA*). The UV/Vis spectral change in Figure 1 upon acetate base concentration

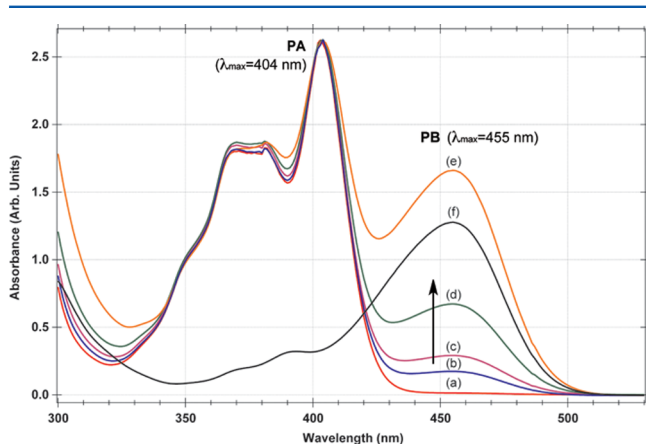


Figure 1. The UV/Vis spectra of 20 mM HPTS dissolved in water with various acetate concentrations. (a) 2 M sodium acetate (NaAc) + 1.26 M acetic acid (HAc), pH = 5.5 buffer solution; (b) 0.1 M NaAc, new; (c) 0.1 M NaAc, used; (d) 0.5 M NaAc, new; (e) 2 M NaAc, new; and (f) 2 M NaAc + 1.26 M HAc + NaOH at pH = 12. All traces except f are normalized to the PA absorbance maximum (404 nm) of trace a. The isosbestic point is at ~ 420 nm. The ~ 50 nm redshift of the absorbance maximum upon PA \rightarrow PB conversion is consistent with the smaller energy gap between PB/PB* than that between PA/PA* of HPTS.

variation is informative. In the most acidic environment of all solutions prepared, 2 M NaAc with 1.26 M HAc maintains the buffer solution pH = 5.5, and the UV/Vis spectrum shows one PA peak with no clear PB population present (Figure 1a). In water solution with 0.1, 0.5, and 2 M NaAc (pH = 7) but no HAc, the relative PB population increases with the increasing acetate concentration because more acetate molecules deprive more protons from PA even in the electronic ground state. The excited state FSRS experiments using a 400 nm actinic pump pulse for several hours increase the PB population to some extent for the 0.1 M acetate sample (Figure 1b \rightarrow c), indicating that some irreversible photoconversion has occurred in the solution. This photoconversion effect is less pronounced in the pH = 5.5 buffer solution, likely due to the excessive protons provided by HAc. In the pH = 12 basic solution with NaOH added, most PA has converted to PB, making PB the predominant form of HPTS in water solution (Figure 1f).

B. Ground State FSRS Spectrum of HPTS. The effective way to identify spectral changes between the PA and PB forms of HPTS is through chemistry, by adding base to deprive the hydroxyl proton of HPTS. The “mild” approach is to vary the concentration of the weak base such as NaAc used in this experiment. It has been widely used by other groups to act as the accepting base for HPTS, mainly due to its suitable pK_a value of 4.8 that falls in between the pK_a of ground state (6.6) and photoexcited (0.0) HPTS. The appearance of HAc signal in the time-resolved measurement of the complex system (see below for excited state FSRS results) can therefore serve as the marker band to correlate the proton motion from the S_1 state of the protonated chromophore (PA*) to the acetate base, along with the generation of the deprotonated chromophore (PB*) still on the S_1 state before its fluorescence to the ground state with a lifetime of ~ 5.3 ns.

Figure 2 shows the comparison between the ground state (S_0) FSRS spectrum of 11 mM PA and PB in water (pH = 6) and NaOH water solution (pH = 12), respectively. Strong peaks above 1000 cm^{-1} are mostly localized ring-H bending motions and bond stretches. There are a number of low-frequency modes at ~ 817 , 667, 465, 435, 290 cm^{-1} that are mainly associated with ring in-plane deformation and ring-H

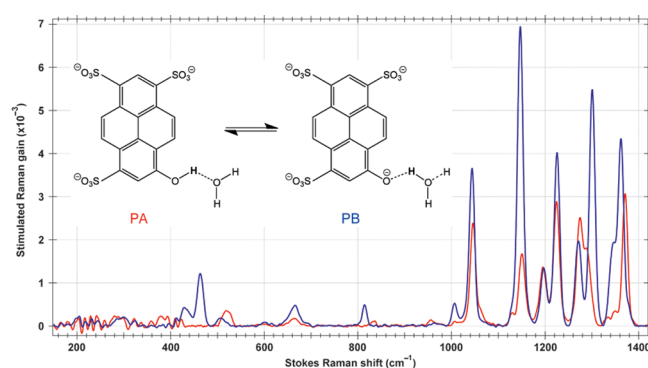


Figure 2. Ground state FSRS spectra of 11 mM HPTS photoacid (PA, red) and its conjugate base (PB, blue) in aqueous solution using the 800 nm Raman pump. The PA form is dominant in water (pH = 6), whereas the PB form is dominant in the strong base NaOH water solution (pH = 12). The chemical structures of the two HPTS forms with a nearby water molecule in different H-bonding geometry are depicted in equilibrium, mainly shifting more negative charge onto the hydroxyl oxygen as the proton transfers to the nearby acceptor molecule.

Table 1. Representative Vibrational Peaks of HPTS in 2 M Acetate Water Solution Observed by FSRS

FSRS peak freq. ^a (cm ⁻¹)	cal. peak freq. ^b (cm ⁻¹)	kinetics of the peak area	major species symbol	vibrational mode assignment
106	111	(+) 640 fs (-) 1 ps (80%); 90 ps (20%)	PA*	HPTS 4-ring OOP wags
150	150	quantum beats with ~260 fs period ^c	PA*	intermolecular O...O stretch between the hydroxyl and the acceptor
195	208	(+) 340 fs (-) 680 fs (80%); 7 ps (20%)	PA*	in-plane ring skeletal breathing with intermolecular O...O bending ^d
321	312	(+) 610 fs (-) 1 ps (85%); 90 ps (15%)	PA*	in-plane ring deformation with some ring HOOPs
445	453 ^e	(+) 700 fs (48%); 27 ps (52%)	PB*	HPTS ring asymmetric wagging motion
1048	1004 ^f	(+) 220 fs (-) 1.6 ps (60%); 45 ps (40%)	PA, PB, PA*	in-plane asymmetric ring-deformation with some CO stretching
1129	1128	N/A	PB	phenolic CO(H) rocking and nearby ring-H rocking
1139	1137 ^e	(+) 220 fs (70%); 30 ps (30%)	PB*	phenolic CO...H rocking and nearby ring-H rocking
1150	1149	N/A	PA	phenolic COH rocking and nearby ring-H rocking
1334	1330 ^e	(+) 430 fs (55%); 11 ps (45%)	PB*	phenolic CO stretch and ring C=C stretch (// to the CO bond)

^aObserved frequencies of the excited state as well as ground state FSRS peaks of 11 mM HPTS in 2 M acetate water solution. ^bRB3LYP-DFT calculations are performed using 6-311G++(2d,2p) basis set for PA-HPTS in solution in complex with a H-bonding water molecule at the phenolic hydroxyl end. Solvent effects are included by the IEF-PCM model. The calculated vibrational frequencies are all with the scaling factor of 0.96. ^cThe kinetics plot is not attempted due to the strong oscillatory pattern of the time-resolved peak integrated intensity (i.e., area) data presented in Figures 7 and S9 up to 3 ps. ^dThis ring skeletal motion specifically modulates the intermolecular (HPTS-)O-H...O(-H₂) angle and distance between the donor and acceptor molecule in the same ring plane. ^eThese PB* modes are approximated using the RB3LYP 6-31G+(d,p) calculation for PB-HPTS in solution in complex with a H-bonding water molecule at the phenolic hydroxyl end (now with a C=O bond). In reality, the excited-state mode of PB* is in a partially deprotonated configuration, and it can significantly deviate from the simple calculation of the corresponding ground-state mode in PB.^fThis rather large discrepancy between the calculated and observed PA, PB mode is interesting, as the calculation correctly captures the trend of this mode being unshifted from PA to PA...H₂O, and from PB to PB...H₂O. So it seems that this mode is relatively insensitive to the electronic distribution over the ring system but deviates from the observed solution configuration. Given that it consists of large-scale in-plane ring deformation and CO stretch at the phenolic end, it probably has a cancellation effect when electrons redistribute. However, this mode intensifies in PB (Figure 2, compared with PA), which agrees with its enhanced Raman polarizability.

out-of-plane (OOP) bending motions. They are generally very weak in S₀ of PA but stronger in PB, probably due to the increased Raman polarizability in a more distorted structure of PB that deviates from the coplanarity of the 4-ring system in PA (discussed later). The molecular structures of PA and PB in different H-bonding geometry with a nearby water molecule are illustrated in the Figure 2 inset.

C. Computational Results for the Vibrational Features of HPTS. Computational chemistry (e.g., vibrational normal-mode analysis) is needed to shed light on the specific molecular motions responsible for the observed vibrational modes. We have first carried out a series of ground-state RB3LYP-DFT calculations⁴¹ using Gaussian 09 with the 6-31G+(d,p) basis set on the HPTS molecule (-3 charge, singlet state) *in vacuo*, and in solution when the solvent effects are included by a polarizable continuum model (PCM) using the integral equation formalism (IEF-PCM). These two calculations yield the respective dipole of 11.5 and 19.1 Debye (D) for HPTS-PA, indicating that the solvation model increases the resulting dipole moment of HPTS. We have also done RB3LYP-DFT calculations with the expanded 6-311G++(2d,2p) basis set and IEF-PCM on the HPTS(PA)...OH₂ complex, which to our understanding better resembles the HPTS molecules in a H-bonding environment. The optimized geometry for the energy minimum is achieved when the water oxygen is in the same

plane with the HPTS ring system, while the two water hydrogen atoms are above and below the ring plane (pointing away from HPTS), respectively. The distance between the phenolic hydrogen and the water oxygen atom is ~1.86 Å, and the OHO angle is ~159°. Note that this angle is not an optimized 180° for the H-bond. This geometry seems to be a reasonable H-bonded configuration in S₀ of HPTS (with a calculated dipole 24.7 D) where the phenolic hydroxyl hydrogens can be H-bonded to either a nearby acetate oxygen or water oxygen atom depending upon the acetate concentration. Mode assignment regarding the observed vibrational modes can be found in Table 1.

Regarding the PB form, calculations are performed on HPTS completely deprived of its proton, hence forming a C=O bond at the ring hydroxyl end, and the total molecule has a -4 charge (calculated dipole 1.27 D). Similar RB3LYP 6-31G+(d,p) calculations on PB (PB...H₂O) with IEF-PCM yield a molecular dipole of 3.31 (6.24) D. It is evident that the solvation increases the charge separation across the HPTS ring system, consistent with the fact that H-bonding plays an important role even in the ground state of protic molecules. Also, there is significant electron delocalization in HPTS-PB than in PA, leading to a greatly reduced dipole moment in the PB form. It is notable that the experimentally accessible PB* form can deviate from the calculated PB form in that the proton

dissociation may not be complete in PB*, and the electronic distribution is not exactly the same for the S_0 and S_1 states, especially for the partially deprotonated form. It is interesting to note that the aforementioned ground-state calculations on PB \cdots H $_2$ O optimize to a configuration in which the nearby water molecule is above the HPTS ring plane, as opposed to the PA \cdots H $_2$ O case that puts the water oxygen in the plane. The calculated distance between the PB phenolic O and the nearby water H is ~ 1.68 Å, and the OHO angle is $\sim 175^\circ$, which is consistent with more electron delocalization and a blueshift of the CO stretching mode.

D. Comparison and Peak Assignment of the Ground State Vibrational Features of HPTS. In the high-frequency region above 1000 cm^{-1} , calculations show ring-H out-of-plane (HOOP) wagging motions close to the phenolic hydroxyl end at 1003 cm^{-1} (PA \cdots H $_2$ O with solvation) and $\sim 990\text{ cm}^{-1}$ (HPTS-PA or PB with solvation) without frequency scaling. This observed HOOP motion at 1008 cm^{-1} is enhanced from PA to PB but remains unshifted as shown in Figure 2. The stronger 1048 cm^{-1} mode shows similar effect from calculations on PA (1046) and PB (1043, all calculated with H-bonding partner and solvation). It is primarily an in-plane asymmetric ring-deformation mode with some CO stretching motion. The mode between $1100\text{--}1180\text{ cm}^{-1}$ can be fitted with a main peak at $\sim 1150\text{ cm}^{-1}$ and a red-shifted shoulder at $\sim 1129\text{ cm}^{-1}$, and PB has a much enhanced peak profile in this region with a main peak redshift by $\sim 3\text{ cm}^{-1}$ (Figure 2). Calculations show an in-plane asymmetric ring-deformation coupled with strong COH rocking (in-plane bending) and some ring-H rocking motions at 1152 (PA, solvation), 1159 (PA \cdots H $_2$ O, solvation), 1147 (PB, solvation), and 1151 cm^{-1} (PB \cdots H $_2$ O, solvation). The next calculated mode with predominantly COH rocking and nearby ring-H rocking motions appears correspondingly at 1186 , 1197 , 1175 , and 1184 cm^{-1} . This higher-frequency mode involves more COH rock that directly modulates the H-bond geometry of HPTS with the nearby acceptor molecule in the ring plane, making it a sensitive probe for the protonation state at the phenolic hydroxyl end of HPTS. It is notable that the simple calculation captures the essence of the observation that upon PA to PB conversion, this COH rocking mode redshifts, and the frequency scaling factor is ~ 0.96 to match the calculation result with experiment (Table 1) for HPTS with H-bonding partners in solution.

The assignment of the doublet band close to 1200 cm^{-1} can be facilitated by its peak separation and intensity ratio change with increasing acetate concentration (Figure 3, dashed lines). The peak separation remains constant ($28.6 \pm 0.5\text{ cm}^{-1}$) with the higher-frequency mode (full-width-at-half-maximum (fwhm) $\sim 17\text{ cm}^{-1}$) gaining relatively more intensity as the population of PB increases, hence leading to higher intensity ratio of the 1227 cm^{-1} mode over the 1198 cm^{-1} mode (fwhm $\sim 21\text{ cm}^{-1}$). This observation is in accordance with the fact that both PA and PB forms exist in HPTS–acetate water solution, and more acetate as efficient proton acceptors corresponds to greater PB population. The larger peak width of the lower-frequency mode can then be attributed to larger inhomogeneity of the PA vibrational transition, as it probably samples more H-bonding configurations than the partially deprotonated PB form of HPTS. These modes are mainly ring-H rocking motions coupled with in-plane ring deformation, with the lower-frequency mode involving bigger COH rocking motions (consistent with its larger inhomogeneity and peak width mainly associated with the PA form).

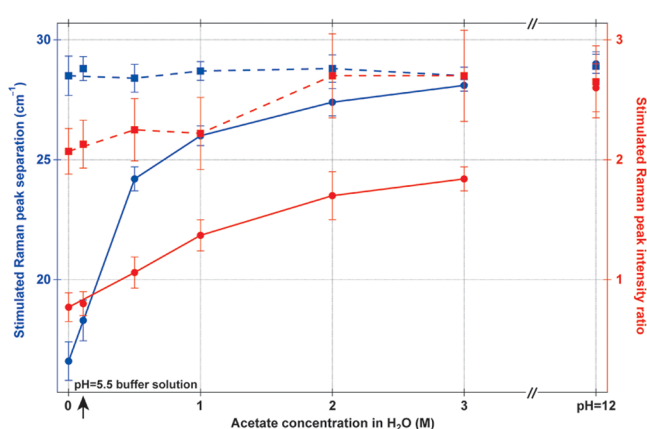


Figure 3. Ground state FSRS data of 11 mM HPTS in water solution with various acetate concentrations. The peak separations between the $\sim 1275/1292$ and $\sim 1198/1227\text{ cm}^{-1}$ peaks are plotted against the left axis (blue) in solid (circles) and dashed (squares) lines, respectively. The peak integrated intensity ratios of the ~ 1292 over 1275 and ~ 1227 over 1198 cm^{-1} peaks are plotted against the right axis (red) in solid (circles) and dashed (squares) lines, respectively. The data in pH = 12 basic NaOH solution where PB is the predominant species are plotted on the right side for comparison, along with the data in the 2 M NaAc+1.26 M HAc buffer solution (pH = 5.5) indicated by a black arrow. The error bar represents one standard deviation from the average value of the parameter from multiple measurements.

The next doublet band between $1250\text{--}1320\text{ cm}^{-1}$ exhibits higher sensitivity to the relative population of PA and PB in solution, and we can confidently assign them to the C–O stretching mode at the ring hydroxyl end. Calculation results with the 0.97 scaling factor are $1250/1312$ (PA, solvation), $1271/1314$ (PA \cdots H $_2$ O, solvation), $1287/1323$ (PB, solvation), and $1285/1325\text{ cm}^{-1}$ (PB \cdots H $_2$ O, solvation). The experimental results are $\sim 1275/1292$ (0 M acetate) and $1272/1301\text{ cm}^{-1}$ (pH = 12) as the peak separations are shown in Figure 3, blue solid line (17 vs 29 cm^{-1}). The calculation of PA \cdots H $_2$ O with IEF-PCM provides good agreement with experiment because it mimics the existing H-bonding network for HPTS in S_0 well, hence the lower frequency for the C–O stretch in the protonated PA \cdots H $_2$ O form matches the observed lower-frequency mode under both pH conditions within 4 cm^{-1} range. The less satisfactory agreement for the higher-frequency mode is likely due to the complexity of the electronic redistribution as the proton transfers away from PA; and the two calculated normal modes for PB can in principle combine or overlap to give the experimental values for the partially deprotonated form, since it is different from the calculated PB modes simply having the C=O bond character. The calculation does show the correct trend in predicting a consistent blueshift of these C–O stretching modes (with some ring deformation, C=C stretch and other ring-H rocks) as the electron cloud becomes more delocalized over the ring system (i.e., 1271 vs 1285 cm^{-1} , 1314 vs 1325 cm^{-1}). As a result, we can attribute the experimentally observed higher-frequency mode to the deprotonated HPTS-PB. In contrast, the lower-frequency mode remains largely unshifted in the experiment, indicating that this mode is mainly associated with HPTS-PA. The intensity ratio of the higher-frequency over lower-frequency mode in Figure 3 steadily increases from below 1 to about 3 with the acetate concentration increase from 0 to 3 M and the pH = 12 solution, which is in excellent agreement with their UV/Vis spectra in Figure 1. The higher the acetate

concentration gets, the higher the percentage is of the PB population in solution. The data from HPTS in 2 M NaAc +1.26 M HAc buffer solution are also plotted in Figure 3, approximately corresponding to a pure acetate concentration of 0.11 M. All those excessive protons in the acidic buffer solution supplied by HAc essentially keep HPTS in pure PA form (Figure 1a).

The doublet between 1320–1400 cm^{-1} consists of a strong peak at 1373 cm^{-1} and a much weaker shoulder at 1350 cm^{-1} in the PA-dominant solution. Upon base addition, the PB-dominant solution shows a red-shifted doublet with a strong 1365 cm^{-1} mode and an increased shoulder at 1347 cm^{-1} . Calculated frequencies with the 0.97 scaling for the ring C=C stretching motions with some ring-H rocking are 1352/1377 (PA, solvation), 1347/1380 (PA \cdots H₂O, solvation), 1332/1345 (PB, solvation), and 1335/1344 cm^{-1} (PB \cdots H₂O, solvation). The redshift of the ring C=C stretching mode is correlated with the PA \rightarrow PB conversion and therefore expected upon photoexcitation, due to further delocalization of the electron cloud over the conjugated ring system as the HPTS acidity increases.

Similar concentrations of HPTS dissolved in several solvents including water, methanol, and dimethyl sulfoxide (DMSO) exhibit the importance of H-bonding on their ground-state FSRS spectra (see Supporting Information, Figure S2). The aprotic DMSO solvent is the least efficient proton acceptor among the three solvents, hence having more protonated HPTS at $\sim 1272 \text{ cm}^{-1}$ for the C–O stretching mode. This mode blueshifts to $\sim 1276 \text{ cm}^{-1}$ in methanol, and further splits into two modes in water at $\sim 1275/1292 \text{ cm}^{-1}$. The ring-H rocking modes around 1200 cm^{-1} also occur at lower frequency in DMSO (1185/1217 cm^{-1}), which represents a redshift of $\sim 5 \text{ cm}^{-1}$ from methanol (1190/1222 cm^{-1}) and $\sim 12 \text{ cm}^{-1}$ from water (1198/1227 cm^{-1}). Peak positions of HPTS in methanol have been compared with the spontaneous Raman measurement using the 647.1 nm line from a Kr⁺ laser ($\sim 100 \text{ mW}$ continuous wave (cw) excitation) on $\sim 50 \text{ mM}$ HPTS (data not shown). The Raman peak positions are well reproduced in FSRS with much better SNR and shorter acquisition time ($< 1 \text{ min}$), but slightly broadened peak width. This implies that the currently used 3.2 ps Raman pump may still truncate a small portion of the vibrational free induction decay tail, and the currently used spectrograph might not achieve the best spectral resolution. This setup will be improved with a new spectrograph.

The comparison between HPTS and MPTS (data not shown) in the same buffer solution (2 M NaAc with 1.26 M HAc at pH = 5.5) lends further support to the vibrational peak assignment. The 1048 cm^{-1} peak of HPTS that is primarily a four-ring asymmetric in-plane deformation mode remains at 1047 cm^{-1} in MPTS. The doublet peaks at $\sim 1271, 1290 \text{ cm}^{-1}$ of HPTS collapses into a single peak at $\sim 1266 \text{ cm}^{-1}$ of MPTS, indicating that the lower-frequency peak can be conclusively assigned to the C–O stretch of the protonated chromophore PA, while the higher-frequency peak is attributed to the C–O stretch of the partially deprotonated chromophore PB as it forms H-bonds with surrounding acceptor molecules (MPTS is clearly deprived of this mode). The proton acceptors are mainly H₂O molecules within solvation shells in low-concentration acetate buffer, but are composed of an increasingly large number of CH₃COO[−] molecules as the acetate concentration goes beyond 1 M (see the doublet peak separation increase in Figure 3). Due to the lack of proton transfer capability of

MPTS, the C–O(–CH₃) stretch assumes purer single-bond character in comparison to the partially delocalized C–O(\cdots H) stretch in HPTS-PA, hence the redshift of $\sim 5 \text{ cm}^{-1}$ (1266 vs 1271 cm^{-1}). This indicates that even the PA form of HPTS is not completely protonated and has some charge separation over the hydroxyl end, shifting more negative charge to the oxygen atom and more positive charge to the hydrogen atom (proton). The doublet peaks at $\sim 1198, 1227 \text{ cm}^{-1}$ of HPTS redshift to $\sim 1187, 1221 \text{ cm}^{-1}$ in MPTS, which are mainly ring-H in-plane rocking and scissoring motions, and the redshift is consistent with the MPTS ring system not H-bonded to nearby acceptor molecules (see calculations above) at the methoxy end. Calculation results on the low-frequency modes will be elaborated in the Discussion section.

E. Excited State FSRS Spectrum of HPTS. It should be noted that the $\sim 11 \text{ mM}$ HPTS molecule described here corresponds to OD $\approx 26/\text{mm}$ at the PA absorption peak ($\epsilon_{\text{PA}} \approx 24\,000 \text{ M}^{-1}\cdot\text{cm}^{-1}$), which is a highly concentrated solution for typical FSRS measurement. It is desirable to have a relatively transparent sample solution such as the previously used OD $\approx 1/\text{mm}$ wtGFP ($\sim 0.4 \text{ mM}$),⁷ but the ground state FSRS spectrum using $\sim 800 \text{ nm}$ Raman pump excitation yields almost no clear peaks for dilute HPTS solution at OD $\approx 1/\text{mm}$. This suggests that the Raman cross-section of the four-ring HPTS is much smaller than the two-ring wtGFP chromophore, likely attributed to the much lower Raman polarizability for the coplanar and rigid structure of HPTS in comparison with the rather flexible two-ring chromophore of wtGFP connected by a C=C–C bridge bond. The highly concentrated HPTS solution gives a nice ground state spectrum but makes the excited state FSRS measurement challenging; since the $\sim 400 \text{ nm}$ photoexcitation pulse is essentially all absorbed within a short distance (a fraction of the 1 mm cell path length) into the sample solution, the OKE signal is carefully adjusted toward the front surface of the cell to aim for maximal photoexcitation. This is where we tweak up the Raman gain signal as well. The incident angle between the actinic pump and Raman probe pulse is reduced to $\sim 5^\circ$ to increase the interaction length between them. Measured from the depth of the dip of the ground-state-subtracted excited state spectra, the maximal population conversion ($S_0 \rightarrow S_1$) that is achieved by $\sim 1.5 \text{ mW}$ of $\sim 400 \text{ nm}$ photoexcitation is $\sim 12\%$.

The excited state FSRS data of acetate water solution only shows flat baselines at all time points, indicating that the 400 nm photoexcitation does not perturb the solvent in our setup. The transient spectral features observed in HPTS or MPTS acetate solutions (or in acetate-acetic acid buffer solutions) are therefore solely due to the absorption of photoexcitation photon energy by the chromophore, and the subsequent ultrafast energy dissipation intra- and intermolecularly across the HPTS ring system involving the surrounding water and acetate molecules.

Figure 4 presents the time-resolved excited state FSRS spectra of 11 mM HPTS and 2 M acetate in water solution following $\sim 1.5 \text{ mW}$ photoexcitation at 400 nm (compressed to $\sim 40 \text{ fs}$), with the 802 nm Raman pump. The ground state spectrum is collected periodically over the whole excited state data collection to monitor sample condition and account for the long-term drift of the laser system. It is then fitted and added back to the ground-state-subtracted excited state transient spectrum using a scaling factor that represents the ground state depletion ratio (Figure S3). After the removal of the spline fit to the broad baseline, the data exhibit an array of

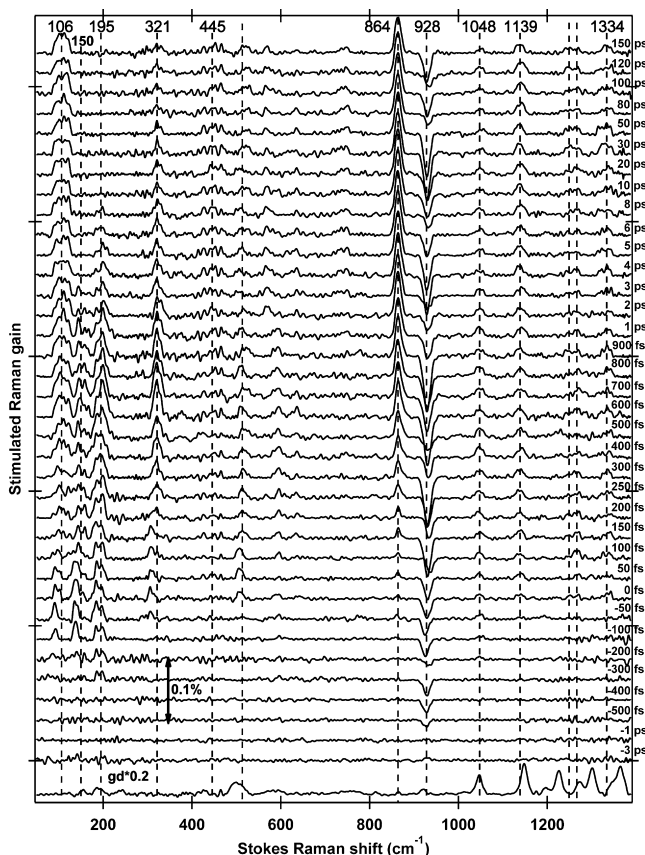


Figure 4. Time-resolved excited state FSRS spectra of 11 mM HPTS with 2 M acetate in water solution following ~ 1.5 mW 400 nm photoexcitation. The Raman pump is at 802 nm. The solvent-removed ground state FSRS spectrum of the sample is scaled and plotted at the bottom. Dashed lines indicate the prominent excited state peaks from both HPTS and the accepting base during ESPT on the femtosecond to picosecond time scale with each time delay labeled on the right side.

positive vibrational features across the spectral range of 100–1400 cm^{-1} with a rich presence of low-frequency modes below 400 cm^{-1} , which are then fitted to a sum of Gaussian peaks. The prominent negative peak at ~ 928 cm^{-1} corresponds to the C–C stretch of the acetate ion, and it is consistent with the ESPT picture that converts more acetate to acetic acid (the positive peak at ~ 864 cm^{-1} , discussion follows) as photoexcited HPTS donates its proton. Additionally, the positive peaks at 1139 and 1334 cm^{-1} are associated with the deprotonated HPTS as its phenolic proton transfers away. It is notable that in comparison to the wtGFP experiments where much stronger excited state Raman peaks were observed due to resonance enhancement,⁷ the current data of HPTS lack this effect, suggesting that PA*-HPTS has no significant transient absorption around 800 nm. The intensity ratio of the excited state peaks (e.g., 1048, 1139 cm^{-1} in Figure 4) to the corresponding ground state peaks is below 10%, which is consistent with the $\sim 12\%$ maximal excitation achieved and also corroborates the lack of resonance enhancement for S_1 peaks. The peak kinetics and the frequency shift from ground state peaks, as well as the intricate relationship between various vibrational modes, exclude the possibility of a simple scheme of Raman pump attenuation-induced ground state depletion.

F. Time Evolution of the Vibrational Modes of Photoexcited HPTS. The ground state depletion ratio (see Figure S3) shows a rise time of 520 ± 80 fs and the biphasic

decay (to $\sim 50\%$ of the maximum depletion) time constants of 1.4 ± 0.2 ps (78% weight) and ~ 100 ps (22%). The subpicosecond rise time is intriguing because the cross-correlation time between the actinic pump and Raman probe is 120 fs, and the vertical excitation into the FC region in S_1 is on the order of 10 fs. The delayed photoexcitation maximum efficiency can be understood as some ultrafast processes (e.g., ≤ 200 fs, stimulated emission) are repopulating the ground state, and that pathway diminishes on the subpicosecond time scale. The double exponential decay of the ground state depletion can be attributed to the recovery of the ground state by internal conversion on the 1–2 ps time scale possibly facilitated by some skeletal motions,²⁷ and by relaxation pathways other than fluorescence (on the nanosecond time scale) likely from a deprotonated chromophore that is generated on the ~ 100 ps time scale.^{13,17} Several peaks are evident in the excited state FSRS spectrum of photoexcited HPTS, and they appear promptly following photoexcitation. The peak intensity of the 1048 cm^{-1} mode rises exponentially with a 220 ± 30 fs time constant and decays with 1.6 ± 0.5 ps (60%) and ~ 45 ps (40%) time constant (Figure 5 and insert).

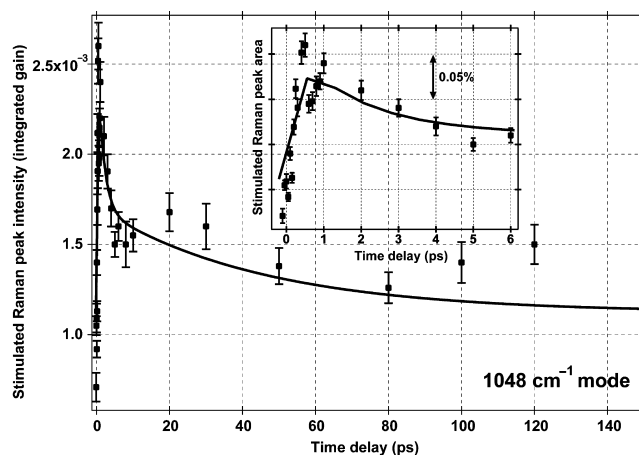


Figure 5. Temporal evolution of the 1048 cm^{-1} excited state mode of 11 mM HPTS with 2 M acetate in water solution following 400 nm photoexcitation up to 150 ps. The peak integrated intensity data are fitted with one rising exponential (~ 220 fs) and two decaying exponentials (~ 1.6 and 45 ps) convoluted with the ~ 120 fs instrument cross-correlation function. The inset shows the very early time dynamics of this PA* mode up to 6 ps. The error bar represents one standard deviation from the average value from multiple fitting procedures of the experimental data.

This mode is assigned to an in-plane asymmetric ring-deformation with some CO stretching motion of PA*, and its frequency remains constant during ESPT in generating PB*.

The 1139 cm^{-1} can be attributed to a modest in-plane ring deformation mode coupled with some CO(\cdots H) rocking of the partially deprotonated HPTS (PB*), which has a different electronic distribution over its ring system from PA (1150 cm^{-1} mode). The calculated PB mode for this motion is ~ 1137 cm^{-1} with solvation and a scaling factor of 0.96, which supports the assignment. The peak area of this mode has a double-exponential rise with 220 ± 30 fs (70%) and ~ 30 ps (30%) time constant. The comparison between the kinetics of the 1139 cm^{-1} mode and the 864 cm^{-1} mode (discussed in detail below) is presented in Figure 6. The fastest component of ~ 220 fs is similar in the appearance of the 1048, 1139 cm^{-1}

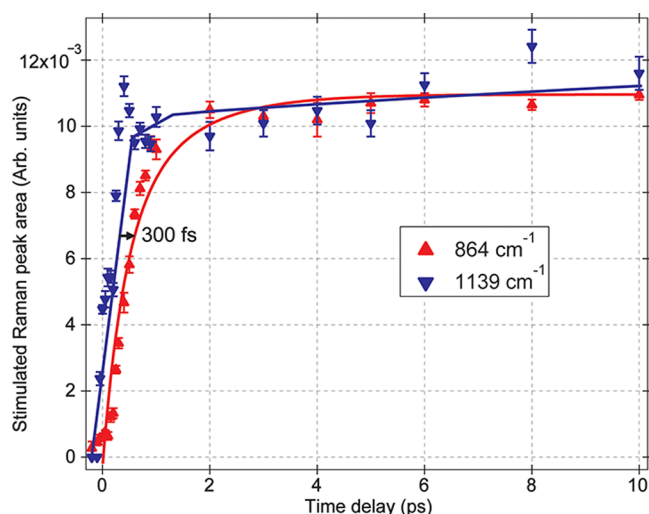


Figure 6. Time evolution of two marker bands for ESPT in 11 mM HPTS with 2 M acetate in water solution up to 10 ps. The 1139 cm^{-1} mode (blue, intensity normalized to the red trace) is assigned to the PB* COH in-plane bending motion that rises earlier and faster than the 864 cm^{-1} mode (red), which is attributed to the C–C stretch of nascent monomer acetic acid. Multiexponential fits are convoluted with the instrument response function (~ 120 fs cross correlation). Error bar represents one standard deviation of the data points. The black arrow marks the delayed onset of the acetic acid signal.

modes, indicating that a portion of the ground-state HPTS molecules is in the “tight” H-bonding configuration that can quickly shift the proton charge toward the acceptor molecule through the strongly polarizable H-bonding chain,^{15,18} inducing significant electronic redistribution over the ring system. This represents the first stage of HPTS dissociation and the initial phase of ESPT.

We also observed excited state peaks at $\sim 1250/1267\text{ cm}^{-1}$ and $\sim 1334\text{ cm}^{-1}$ that promptly appear following photoexcitation. They represent a blueshift from the ground state peaks at $\sim 1227\text{ cm}^{-1}$ and 1302 cm^{-1} , which can be attributed to the fast electronic redistribution with the slower charge transfer from the hydroxyl oxygen to the aromatic rings induced by the proton departure from HPTS. DFT calculations (Table 1) lend support to this mechanism, and we can assign them as PB* modes mainly involving the ring C=C stretch coupled with C–O(\cdots H) stretch. The peak area of the 1334 cm^{-1} mode has a biphasic exponential rise with time constants of ~ 430 fs (55%) and ~ 11 ps (45%), which reports on the time scale for the blueshift of the C–O stretch band. The magnitude of this $\sim 32\text{ cm}^{-1}$ blueshift is smaller than the $\sim 45\text{ cm}^{-1}$ observed during ESPT in wtGFP,⁷ suggesting that the degree of ground-state deprotonation is larger in the HPTS-acetate-water system, which has abundant H-bonding partners to HPTS (compared with limited H-bonding options in the hydrophobic protein pocket of wtGFP). This vibrational band involves larger-scale localized motions of heavier atoms (e.g., oxygen atom) than the 1139 cm^{-1} mode, therefore showing a delayed onset (430 vs 220 fs). The appearance of the blueshifted C–O stretch is a staple for the charge transfer from the hydroxyl group to the aromatic ring system, and is likely accompanied by some ring skeletal motions (see below discussion) to stabilize this charge.

Figure 7 presents the time evolution of five prominent low-frequency modes from the excited state FSRS data in Figure 4. The peak intensity of the 106 cm^{-1} mode rises exponentially with a 640 ± 60 fs time constant and decays with ~ 1 ps (80%)

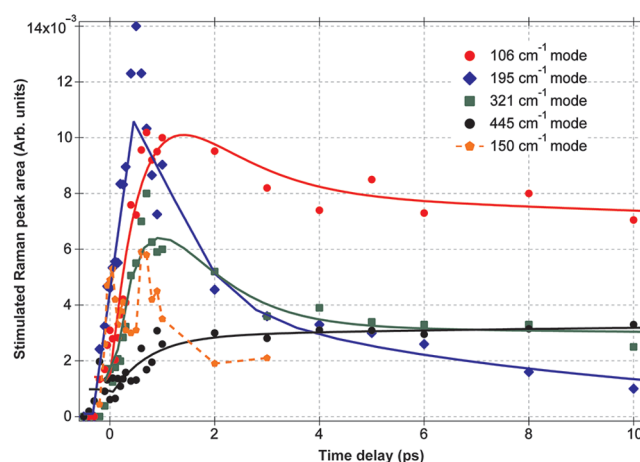


Figure 7. Temporal evolution of the excited state low-frequency modes of 11 mM HPTS with 2 M acetate in water solution following 400 nm photoexcitation. The stimulated Raman peak intensity is obtained from the integrated Raman gain as shown in Figure 4, and the solid lines are multiexponential fits to the plotted data for each mode convoluted with the 120 fs cross-correlation function. Due to the strong oscillatory pattern of the 150 cm^{-1} mode, a convoluted multiexponential fit was not performed, and the orange dashed line simply connects the data points to show the fast rise (comparable with the 195 cm^{-1} mode) and strong oscillatory pattern of this mode following electronic excitation.

and 90 ps (20%) time constant. The 321 cm^{-1} mode has a rising component of 610 ± 40 fs and a decaying exponential with ~ 1 ps (85%) and 90 ps (15%) time constant. The remarkably similar dynamics suggest that these two low-frequency modes with delayed onset share similar structural origin and are associated with some “intermediate” structures of the photoacid PA* that are actively transferring the proton away. The 195 cm^{-1} mode, on the other hand, shows distinctive dynamics from the aforementioned two low-frequency modes. Following photoexcitation, this mode rises with 340 ± 50 fs time constant and decays biexponentially with two time constants of 680 ± 70 fs ($\sim 80\%$) and 7 ± 1 ps ($\sim 20\%$). The modes between $400\text{--}800\text{ cm}^{-1}$ are primarily ring deformation modes (in-plane bending and breathing, OOP wagging) and they appear promptly after photoexcitation except the mode at $\sim 742\text{ cm}^{-1}$. The $\sim 445\text{ cm}^{-1}$ mode is a signature band of PB that consists mostly of ring asymmetric wags ($\sim 472\text{ cm}^{-1}$ with IEF-PCM-water calculation on PB \cdots H₂O, unscaled). The excited state FSRS data in Figure 4 show the gradual appearance of this PB* mode following photoexcitation, with the rising time constants of 700 ± 40 fs (48%) and 27 ± 10 ps (52%) as plotted in Figure 7. Preliminary excited state FSRS experiments on MPTS have also been carried out for comparison with HPTS.

IV. DISCUSSION

The ultrafast vibrational spectroscopic approach with the simultaneously high spectral and temporal resolution provided by FSRS has enabled us to observe the previously hidden multidimensional reaction coordinate of the excited state potential energy surface (PES) of HPTS. The photoacid has weak ground state Raman features with the off-resonance 800 nm Raman pump, and no significant transient absorption from S₁ to higher-lying electronic states to augment the excited state peaks. However, we use highly concentrated samples (~ 11 mM

HPTS) and relatively intense photoexcitation pulse (~ 40 fs, ~ 1.5 mW) to obtain the excited state Raman features of HPTS reporting on its conformational dynamics during ESPT on the femtosecond to picosecond time scale (Figure 4). The proton transfer and charge transfer processes⁴² can then be respectively scrutinized in detail. For instance, the translocation of the proton through the H-bonding chain will be probed by the dynamics of the nascent acetic acid peak at the proton acceptor site. This process is accompanied by the vibrational normal modes of HPTS that are associated with a different electronic configuration from S_0 . By contrast, the transfer of the negative charge now residing on the HPTS hydroxyl oxygen back to the aromatic ring system might lag behind, which can be reflected by the kinetics of the blueshifted phenolic C–O stretch peak. These marker bands and their implications in the context of multidimensional reaction coordinate for ESPT will be discussed next.

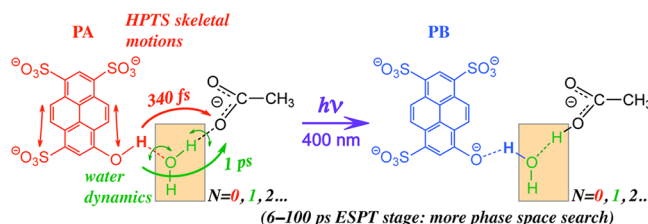
Assignment of the Nascent Acetic Acid Monomer Peak As a Marker Band for ESPT. The comparison between the pH = 5.5 buffer solution and the pH = 12 same buffer solution but with NaOH to shift all the equilibrium toward acetate ions shows the clear existence of a 864 cm^{-1} mode in the acidic environment (Figure S4). RB3LYP-DFT calculations on a $\text{HAc}\cdots\text{H}_2\text{O}$ complex with 6-311G++(2d,2p) basis set and IEF-PCM-water treatment predict a dipole moment of 2.67 D and the symmetric CH_3 deformation mode at 1393 cm^{-1} , which corresponds to our experimental value at 1368 cm^{-1} (see Figure S5). So the scaling factor to use is ~ 0.98 , and the C–C stretch calculated at 882 cm^{-1} then corresponds to $\sim 864\text{ cm}^{-1}$, which excellently matches our experimental value. DFT calculations at the same level for HAc dimer (0.005 D dipole) show the C–C stretch at $902/906\text{ cm}^{-1}$ that represents a blueshift from the corresponding monomer peak.

The ground-state FSRS spectra of the acetic acid water solution with varying HAc concentrations lend further support to the assignment of the $\sim 870\text{ cm}^{-1}$ mode (Figure S5). The multipeak Gaussian-profile least-squares fitting of the main acetic acid peak in water solution consistently yields three spectral components at 872 , 890 , and 912 cm^{-1} , with the middle peak having the largest intensity. The intensity (area) partition of the three peaks is 4.7%, 89.4%, 5.9% in 0.5 M HAc water solution, 5.2%, 88.7%, 6.1% with 1 M HAc, 4.8%, 90.7%, 4.5% with 2 M HAc, and 4.2%, 90.5%, 5.3% with 4 M HAc, respectively. According to the literature^{43–45} and our DFT calculations *in vacuo*, this mode is primarily the C–C stretching band with the medium-intensity $\sim 851\text{ cm}^{-1}$ mode attributed to the monomer, and the very strong $\sim 892\text{ cm}^{-1}$ attributed to the dimer.⁴⁴ The acetic acid gaseous and solution phase Raman spectra provide useful comparison, and the blueshift of the monomer peak upon solvation ($851 \rightarrow 872\text{ cm}^{-1}$) can be understood, as the HAc molecule interacts with surrounding water molecules, the electronic delocalization shifts some electron density to the C–C bond, hence increasing its stretching frequency. On the contrary, the dimer structure remains constant going from the gas phase to the condensed phase, so the 892 cm^{-1} mode stays at the same frequency. In the buffer solution with $\sim 1.6:1$ NaAc:HAc composition at pH ≈ 5.5 , more HAc monomer is present derived from the equilibrium between HAc and monomer acetate ion, and the peak fitting yields an intensity partition of 12% and 88% for the 864 and 894 cm^{-1} modes, respectively (Figure S4). It is conspicuous that the acetate ion used as the acceptor in our FSRS experiments receives the proton transferred from HPTS

and only generates monomer HAc on the picosecond time scale, so the nascent HAc peak at $\sim 870\text{ cm}^{-1}$ serves as a clear marker band for the ESPT progress.

The excited state FSRS spectra show that the 864 cm^{-1} mode appears on the subpicosecond time scale with a fitted single exponential growth time constant of 530 ± 50 fs. Compared with the ~ 220 fs rise time of the 1139 cm^{-1} PB^* mode, the monomer HAc peak has a delayed onset of ~ 300 fs (Figure 6). This is a very interesting result because it does not agree with the simple interpretation that a single-stage ESPT leads to the proton moving from HPTS to the tightly bound acetate ion; otherwise, the HAc peak should display similar dynamics with the PB^* mode. It is notable that the acetate dip intensity at 930 cm^{-1} in Figure 4 also shows interesting dynamics that can be fit to a quick drop (500 ± 50 fs) and a biphasic slow recovery (630 ± 60 fs, 85% and ~ 60 ps, 15%). The dominant peak intensity drop time constant of 500 fs associated with the acetate ion correlates nicely with the weighted acetic acid signal increase (530 fs), evident that the acetate acts as the main proton acceptor on this time scale. And the dominant acetate peak recovery time constant of 630 fs matches well with the activation of the 106 and 321 cm^{-1} modes (rise time constants of 610–630 fs, see below). We suspect that the nascent acetate dip and acetic acid peak involved with the ESPT reaction might be significantly enhanced, due to the disruption to their original relaxed H-bonding configuration (i.e., in S_0) by photoexcited HPTS and the subsequent increase of their electronic polarizabilities. A multistaged ESPT (Scheme 1) along a

Scheme 1. Multidimensional Reaction Coordinate and Multistaged ESPT Reaction of Photoexcited HPTS in Acetate Water Solution



multidimensional reaction coordinate through various-length H-bonded chains is capable of explaining this phenomenon, and the structural dynamics information is directly embedded in the low-frequency region of the FSRS data.

Structural Dynamics of ESPT Inferred from Distinctive Evolution of Various Low-Frequency Modes. It is remarkable that the time-resolved excited state FSRS spectra in Figure 4 exhibit an array of active low-frequency modes promptly following photoexcitation. Their temporal evolution particularly on the femtosecond to picosecond time scale is accompanied by ESPT, which is evident from the time evolution of a number of high-frequency modes associated with the proton donor and acceptor. The simultaneous measurement of all the active normal modes involved with the chemical reaction (e.g., ESPT here) *in situ* provides rich information not readily available from conventional Raman experiments or transient absorption measurements. In particular, low-frequency modes are generally challenging to obtain using Raman spectroscopic techniques because they require probe photons to be very close in wavelength to Raman pump photons, which are much stronger in intensity and also producing strong Rayleigh scattering. The femtosecond laser

system that we use further complicates the situation by having ultrafast pulses very broad in the frequency domain. In order to detect low-frequency modes of photosensitive molecules, a stable white light needs to be generated in the vicinity of the Raman pump fundamental currently set at ~ 800 nm for our apparatus. As a result, a 300 cm^{-1} mode corresponds to ~ 820 nm probe photon that is largely cut off by the RG830 long-pass filter. However, the Raman probe pulse can be carefully adjusted to achieve a smooth spectral shape imaged onto the CCD detector, to enable the *simultaneous* observation of low- and high-frequency modes as the probe spans from 805 to 905 nm, and to elucidate the correlation between various vibrational modes associated with different parts of the molecule. It is not the mere fact that they exist but the temporal evolution of the observed excited state vibrational modes that forms the foundation of our interpretation and understanding of the reaction mechanism.

DFT calculations on HPTS show a four-ring OOP wagging motion at 121 cm^{-1} (*in vacuo*) and 116 cm^{-1} (IEF-PCM-water, with or without the complexed water molecule) that brings the hydroxyl group above and below the coplanar four-ring plane in S_0 . The calculated frequencies are unscaled unless otherwise stated (Table 1). The calculation also shows a predominantly OOP wagging motion of the hydroxyl proton (HOOP) at 295 cm^{-1} (*in vacuo*) that blueshifts to 351 cm^{-1} under IEF-PCM-water treatment. Interestingly this mode stays at 292 cm^{-1} for the $\text{PA}\cdots\text{H}_2\text{O}$ complex under IEF-PCM-water treatment, except that some significant water H-rocking motions are involved therein. The 325 cm^{-1} mode of $\text{PA}\cdots\text{H}_2\text{O}$ is a ring in-plane deformation mode that modulates the intermolecular distance between the HPTS hydroxyl group and the complexed H_2O molecule. The nearby 368 cm^{-1} mode of $\text{PA}\cdots\text{H}_2\text{O}$ is an in-plane ring rocking mode that predominantly involves a scissoring motion between the phenolic hydroxyl and the nearby ring-H. Calculations tend to give relatively accurate frequencies for low-frequency modes due to the nature of those collective skeletal motions, which also do not change their vibrational frequencies significantly upon electronic excitation.^{7,24,25} The common feature of these low-frequency modes is that they both adjust the relative geometry between the donor (HPTS) and nearby acceptor (water or acetate), and they involve relatively large-scale atomic motions such as the four-ring OOP wagging, HOOPs, and the hydroxyl group bending motions. This finding explains their ~ 630 fs rise time (in PA^*) that is longer than the ~ 220 fs appearance of the PB^* peak at 1139 cm^{-1} , which is a modest in-plane ring deformation mode with stronger localized $\text{CO}(\cdots\text{H})$ rocking of the partially deprotonated HPTS, resulting from an ultrafast proton transfer along the preformed HPTS-acetate H-bond in the four-ring plane.

The fastest rise time of the 195 cm^{-1} mode among all the observed low-frequency modes indicates that the associated atomic motion is easier to access by photoexcitation, with the excited wavepacket probably still in the A^* FC region. This suggests that it is more likely to be an in-plane skeletal mode rather than an OOP mode. DFT calculation of HPTS *in vacuo* indeed shows an in-plane ring skeletal breathing motion at 208 cm^{-1} that displaces the hydroxyl group in the ring plane but without COH bending (this calculated mode blueshifts to 215 cm^{-1} under IEF-PCM-water treatment, and to 217 cm^{-1} when a water molecule is H-bonded to the hydroxyl group of HPTS). Note that the aforementioned optimized S_0 geometry for $\text{PA}\cdots\text{H}_2\text{O}$ has an OHO angle of $\sim 159^\circ$, and this normal mode

actually brings the hydroxyl into better H-bonding configuration with the nearby water molecule along its trajectory. It is therefore reasonable to associate this PA^* mode with the first stage of ESPT, where the proton simply moves toward the acceptor in the ring plane, along the highly polarizable H-bond chain initially formed in the ground state and better aligned by the 195 cm^{-1} mode. The reaction coordinate hence involves HPTS configurations that do not differ significantly from the S_0 equilibrium geometry that is coplanar for the aromatic ring system. The photoactivated 195 cm^{-1} mode of PA^* mainly facilitates the translational motion of the proton through the preformed $\text{HPTS}-\text{O}^-\cdots\text{H}^+\cdots\text{OOCCH}_3$ chain to generate the 1139 cm^{-1} mode of PB^* and some HAc (not all) on the ~ 220 – 340 fs time scale.

As HPTS continues to adjust its relative geometry with the nearby “rearranging” water molecules to transfer protons that are not optimally bound between HPTS and acetate ions, it gradually breaks the initial ring planarity and shifts the negative charge on the hydroxyl oxygen toward the rings, leading to the diminishing intensity of the 195 cm^{-1} in-plane mode. Interestingly, its dominant decay time constant of 680 fs matches very well with the rise time of two other PA^* modes at 106 and 321 cm^{-1} (~ 630 fs, Table 1), indicating that these ring wags and hydroxyl HOOP motions are activated *after* the in-plane ring breathing motions. The remaining 20% of the 195 cm^{-1} mode intensity decay has a ~ 7 ps time constant, which might be associated with the photoexcited HPTS bringing more water/acetate molecules into optimal geometry with the further twisted HPTS to continue transfer more protons. This process is through the increasingly extended H-bond chain with further optimized heavy atom configuration for ESPT and PB^* production. The ~ 7 ps decay constant of the 195 cm^{-1} mode is significantly shorter than its counterpart in the 106 and 321 cm^{-1} modes (~ 90 ps), indicating that HPTS twists away from the ring coplanarity facilitated by ring wags and hydroxyl HOOPs in several ps and does not return to the coplanar structure within our experimental time window (up to 150 ps). At this time, most of the excited state HPTS population is in PB^* , consistent with the second rise time constant of the blueshifted C–O stretching mode at ~ 11 ps. On the contrary, there are still activities of the 106 and 321 cm^{-1} modes at the longest time delay measured (150 ps), implying that these two OOP modes accompany ESPT all the way but with strongest activity on the ~ 1 ps time scale to facilitate proton conduction via one intervening water molecule. In addition, the peak frequency of the 195 cm^{-1} mode shows a biphasic exponential increase with ~ 520 fs (90%) and ~ 5.5 ps (10%) toward $\sim 201\text{ cm}^{-1}$, which implies that this particular in-plane ring breathing mode is strongly affected by the activation of the other two ring wagging modes in PA^* , and the blueshift is consistent with the aforementioned calculations on PA and PB .

The dominant decay time constant of the 106 and 321 cm^{-1} modes being ~ 1 ps merits some discussion. This is very close to the proton hopping time of 1.3–1.5 ps over a single water molecule in pure water,^{18,46} as well as the water molecule reorientation time (~ 1.5 ps) at room temperature.^{47,48} The fact that these two low-frequency modes are mostly active on the ~ 1 ps time scale implies a significant subpopulation of HPTS in S_0 that H-bonds to an acetate ion via an intervening water molecule; once these protons are transferred through, there will be less hydroxyl HOOP contributions to these wagging motions, and it takes longer for them to sample phase space and establish more H-bonding chains. Further solvent

rearrangement and/or acetate diffusion are then needed to continue ESPT on the tens to hundreds of picoseconds time scale. Approximately as a back-of-the-envelope calculation, if we take the rise time constant of 220 fs (70% weight of the total signal rise of the PB* mode at 1139 cm^{-1}) that is attributed to the initial phase of direct ESPT through the preexisted HPTS–O[−]...H⁺...[−]OOCCH₃ chain, and the rest 30% being the dominant ~ 1 ps decay time for both 106 and 321 cm^{-1} modes that facilitates ESPT through one intervening H₂O molecule, we obtain a weighted average of ~ 450 fs for the HAc signal rise. This agrees reasonably well with the observed ~ 530 fs rising exponential of the HAc peak plotted in Figure 6. If we replace the 220 fs time constant with the 340 fs rise time of the 195 cm^{-1} mode, the weighted HAc generation time is 540 fs, which is even closer to the observed value. This signifies the importance of these low-frequency modes in facilitating ESPT by optimizing the donor–acceptor geometry through skeletal vibrations and various H-bonding chains. We can also fit the HAc signal rise using double exponentials, and get ~ 400 fs (60%) and ~ 1.2 ps (40%), and the fitting residual is comparable to the single-exponential fit if not better.

It is notable that the frequency of the HAc peak also shows multiexponential dynamics (Figure S6) with a 320 ± 40 fs rise, and two decay time constants of 550 ± 60 fs (60%) and ~ 90 ps (40%). Since this mode frequency is sensitive to the immediate environment of HAc, we can attribute the rise time to be the solvation of nascent HAc from the initial phase of ESPT involving the tight HPTS–acetate complex, and the first decay time constant to the water molecular rearrangement within the loose HPTS...H₂O...acetate complex to achieve optimized geometry for the second phase of ESPT.

Other Low-Frequency Modes Reporting on the Conformation Dynamics of the HPTS Ring System. It is plausible that as the proton transfers away from the chromophore on the femtosecond to picosecond time scale, the initial coplanarity among the conjugated ring structure in S₀ is gradually broken. This corresponds to an excited state structure that loosens its hold onto the hydroxyl proton that is initially part of the planar conjugated ring system. Remarkably, the 700 fs rise time constant of the $\sim 445\text{ cm}^{-1}$ mode (Table 1 and Figure 7) once again matches very well with the 650 fs rise of the PA* modes at 106 and 321 cm^{-1} , as well as the dominant ~ 680 fs decay of the 195 cm^{-1} mode also in PA*. This observation signifies that this type of collective ring wagging motions in PA* project strongly onto the reaction coordinate responsible for the photoacidity of HPTS on the >500 fs time scale, likely out of the FC region along the associated nuclear coordinates throughout ESPT to generate PB*.^{7,25} The skeletal wagging motions occur after the initial phase of ESPT on the ~ 300 fs time scale when the 195 cm^{-1} in-plane ring breathing is the most active low-frequency mode, which primarily modulates the intermolecular distance between the hydroxyl group of HPTS and the bound base. The 195 cm^{-1} mode is therefore prone to be activated along the steep slope within the FC region following photoexcitation.

The 27 ps rise time of the 445 cm^{-1} ring asymmetric wags agrees well with the second rise time constant of the 1139 cm^{-1} mode (30 ps), albeit with more weight responsible for the overall peak rising dynamics (52% vs 30% in 1139 cm^{-1}). Both modes are associated with PB* configurations, but the in-plane mode rises and decays faster than the OOP wagging mode. The second rise time of the 1334 cm^{-1} C–O stretching mode at 11 ps (45% weight, Table 1) is the most transient among these

PB* modes, implying that changes to the hydroxyl group are completed following proton departure, while the aromatic ring system continues to evolve on the tens to hundreds of picoseconds time scale to stabilize the nascent PB* electronic configuration. The ring system continues to search phase space for the remaining ESPT channels before fluorescence on the nanosecond time scale.

The 674 cm^{-1} mode in the PA ground state slightly redshifts and intensifies as the PB concentration increases. DFT calculations on PA...H₂O with IEF-PCM-water show a four-ring symmetric breathing motion with small OOP motions in the vicinity of it ($\sim 663\text{ cm}^{-1}$ unscaled). Similar calculation on PB with IEF-PCM-water shows the mode at 660 cm^{-1} . The PB accumulation correlates with more lost planarity among the four rings and hence the mixture of in-plane with OOP modes to a greater extent, consistent with the redshift of the 674 cm^{-1} mode. It is much less prominent than the $\sim 445\text{ cm}^{-1}$ wagging mode in excited state FSRS (after 1 ps, see Figure 4) due to the Raman polarizability difference, evincing that the wagging mode is more relevant for the ESPT reaction coordinate and more actively involved in facilitating ESPT on the picosecond time scale.

The current data set has reduced SNR in the low-frequency region of the ground state data due to some interference patterns below 500 cm^{-1} on the CCD, and we suspect that the Raman pump might have generated some continuum light to act as a local oscillator pulse for the Raman probe. Additionally, the residual 800 nm fundamental pulse used to generate the Raman probe continuum also contributes to some interference effect. The removal of these interferences through filtered FFT techniques reveals several low-frequency modes that match well with the aforementioned FSRS data analysis. The pattern remains largely stable during the course of the experiment, so the ground-state subtraction works well to obtain excited state Raman spectra in Figure 4. However, eliminating the interferences would surely improve our SNR. We also see a broad 490 cm^{-1} signal in the empty quartz cell. More data with comparison of the strength and evolution of low-frequency modes of photoexcited HPTS with increased SNR will be published in the future, with a targeted smoother white light profile below 500 cm^{-1} . The preliminary data show that the $\sim 450\text{ cm}^{-1}$ mode is more prominent in HPTS water solution with higher acetate concentration (e.g., 2–4 M), consistent with the more twisted molecular conformations of HPTS that accommodate more H-bonds with surrounding acetate molecules as proton acceptors.

Spectral Change of HPTS upon Light-Emitting Diode (LED) Illumination. We have also investigated HPTS using steady state spectroscopy. Continuous illumination of the sample cell using 395 nm LED light causes the increase of the peak intensity from 260–600 cm^{-1} , which corresponds to a number of ring OOP wagging modes of HPTS (Figure S7). It signifies a loss of the ring coplanarity of the ground state as the molecule absorbs energy from the photoexcitation light. The LED light source is much lower in peak intensity compared with the femtosecond 400 nm pulse used for excited state FSRS, so even though it is continuous and has ~ 15 mW average power, we did not observe a clear population shift from PA to PB as confirmed by the constant intensity ratio between the ~ 1275 and $\sim 1302\text{ cm}^{-1}$ modes. Also, the ground state depletion is likely due to the local heating effect at the sample spot that shifts the transmitted Raman probe direction to some extent, hence the decrease of PA peak intensity. However, the

skeletal motions do become more active in response to a twisted structure deviated from the ground state coplanar geometry of HPTS. Another control experiment was done for 11 mM HPTS in NaOH water solution (pH = 12) under continuous illumination by 455 nm LED light (Figure S8). Since the HPTS molecule is predominantly deprotonated in this highly basic environment, the spectral changes induced by the low-power cw light are negligible in the high-frequency region ($>1,000\text{ cm}^{-1}$, no significant PA \rightarrow PB conversion therein) but non-negligible in the low-frequency range. Two low-frequency modes stand out, at ~ 375 and 526 cm^{-1} , which agree reasonably well with the calculated PB modes at ~ 391 and 529 cm^{-1} (scaling factor 0.96) mainly associated with four-ring OOP wags and HOOP motions. This observation indicates a further distorted structure of HPTS as the deprotonated chromophore absorbs the incoming photon energy and commits more collective skeletal motions to dissipate the photoexcitation energy.

Comparison of the FSRS Excited State Spectra of MPTS with HPTS. It is interesting to mention that in MPTS, which does not have proton transfer capability due to the replacement of the phenolic hydroxyl group with a methyl group, the fluorescence upon 400 nm excitation is in the blue, which indicates that it is likely a downward transition from PA* directly back to PA (larger energy gap than PB* \rightarrow PB). Using similar pump power ($\sim 1.5\text{ mW}$), we observed that the MPTS solution quickly gets murky and nontransparent, which suggests that the high peak energy of the photoexcitation pulse irreversibly converts MPTS into some other state, or aggregation occurs. The preliminary FSRS data of MPTS retrieved from the sample solution before it degrades show ground state depletion for modes above 1000 cm^{-1} and a number of positive-going excited state peaks mostly below 600 cm^{-1} with frequencies and kinetics different from HPTS. This observation corroborates the hypothesis that these photo-sensitive conjugated-ring systems exhibit various ring deformation motions following electronic excitation to navigate the S_1 state landscape of PA* or PB* before radiative relaxation (fluorescence) back to S_0 . Further experiments with optimized optical setup and less photoexcitation power should provide a clear comparison between active low-frequency modes primarily associated with S_1 of MPTS and HPTS, helping us identify the key skeletal motions that strongly modulate proton motion through PA* and PB*, and hence efficiently facilitate ESPT in HPTS but not in MPTS.

Multidimensional Nature of the ESPT Reaction Coordinate. The current data of 11 mM HPTS and 2 M acetate in water solution represent a water-deficient environment around HPTS in which the direct proton transfer from the photoacid to the conjugate base in the tight and loose complexes dominates the initial reaction dynamics of ESPT. There have been a large number of reports concerning the preformed H-bonds in the ground state of photosensitive chromophores and the almost barrierless ultrafast ESPT upon photoexcitation.^{14,30} It is generally accepted that ESPT through those short-distance (e.g., O \cdots O distance $< 2.4\text{ \AA}$) donor–acceptor H-bond already formed in the ground state is on the order of 100–200 fs, which typically represents a tight complex such as HPTS–O \cdots H $^+$ \cdots –OOCCH₃ with no intervening water molecules in our system. Even faster ESPT processes that typically occur within 100 fs have been associated with coherent type of proton motions due to photoexcitation, possibly determined by the low-frequency motion and its vibrational

period.²¹ Immediately following 400 nm photoexcitation, HPTS-PA loosens its hold of the hydroxyl proton that is already in some H-bonding geometry with a nearby acetate molecule, and the proton conduction to the base is accompanied by the initial electronic redistribution over the HPTS ring system. As the excited wavepacket moves out of the FC region of A*, the 220 fs rise time of the 1139 cm^{-1} mode that represents a redshift from the 1150 cm^{-1} PA mode is a staple of the fastest PB* generation. It is notable that this 220 fs rise time is larger than the previously reported rise time of $\sim 150\text{ fs}$ for acetic acid generation in a similar system,¹⁵ but the difference can be attributed to the nature of the proton-coupled electron transfer. The almost barrierless proton transfer to the acetate ion through the preformed H-bonding chain might occur within 150 fs to start producing the monomer acetic acid, but the appearance of the 1139 cm^{-1} PB* mode needs to involve more collective motions of the HPTS heavy atoms and hence slightly lags behind. The 195 cm^{-1} in-plane ring skeletal breathing motion of PA* then catches up and displaces the hydroxyl proton in the ring plane (but without COH bending) on the 340 fs time scale. This nuclear motion accompanies the initial phase of ESPT through the tight HPTS–acetate complexes via no intervening water molecule (see Scheme 1).

The delayed onset of the 106 and 321 cm^{-1} modes ($\sim 630\text{ fs}$ rise time) marks the beginning of the second phase of ESPT that transfers proton through the HPTS–OH \cdots H₂O \cdots –OOCCH₃ complex. At this time, the negative charge on the hydroxyl oxygen is much less stabilized after the initial phase of ESPT, and more energy dissipation among the ring system starts to break the four-ring coplanarity and activate the OOP wagging motions of both ring-carbons and ring-hydrogens. Meanwhile the 195 cm^{-1} in-plane mode diminishes. This movement correlates nicely with the solvent rearrangement in the immediate vicinity of HPTS, namely the water molecule that is initially loosely bound in between HPTS and acetate but not in a favorable H-bonding configuration. The ring wagging motions facilitate the optimization of this H-bonding chain and efficiently conduct the proton on the 1 ps time scale,⁷ consistent with the Grotthuss hopping time for intermolecular proton transfer via a single water molecule in pure water.^{17,18,46–48} The first decay time constant of the 1048 cm^{-1} PA* mode at 1.6 ps also probes this specific process. These two early stages of ESPT with distinctive time scale give a weighted acetic acid production time of $\sim 540\text{ fs}$ that is in excellent agreement with the observed value of $\sim 530\text{ fs}$ for acetic acid appearance and $\sim 500\text{ fs}$ for acetate disappearance. Near the completion of the second phase of ESPT, the two ring wagging and ring-H HOOP motions at 106 and 321 cm^{-1} begin to diminish but remain active to facilitate further ESPT.

A slower component on the time scale of 6 to several tens of picoseconds is assigned to ESPT in solvent-separated HPTS–acetate “loose” complexes like HPTS–OH \cdots (H₂O)_{*n*} \cdots –OOCCH₃ ($n \geq 2$) that probably involves the rearrangement of multiple solvent molecules and/or acetate molecules to optimize the ESPT efficiency. Recent reports on the role of water in intermolecular proton transfer reactions argued that translational diffusion of the reactants is not essential for reactant separations larger than one water molecule; instead the solvent configuration search to establish a more efficient H-bonding chain is more relevant for the process.^{18,19} Since the ring wags and ring-H HOOP motions remain active on this time scale (up to 150 ps measured in this work), and the PB* peak at 445 cm^{-1} gets stronger, HPTS is in a twisted geometry

away from the coplanar ring configuration and has a better chance to sample more phase space to establish optimal H-bonding geometry, while waiting for acceptor heavy atoms to align through the extended H-bonding chain.⁷ The PB* peaks at 445 (1139) cm^{-1} with the ~ 27 (30) ps rise time along with the PA* peak at 1048 cm^{-1} with the ~ 45 ps decay time constant can be viewed as representative modes on this ESPT stage across longer H-bonding chains between HPTS and base.

It is our understanding that there is still a debate in the theoretical chemistry field of whether charge transfer precedes or lags behind proton transfer, and our current data have offered some new insights into this intricate process. The early stage electron transfer (i.e., electronic redistribution that deviates from the ground state configuration) mainly results from the coherent proton motion between the tautomeric states^{7,21} of the preformed H-bonded HPTS–acetate complex. If we take ~ 150 fs as the earliest rise time constant for acetic acid, then the electron transfer toward the HPTS ring system might take a bit longer to occur with a 220 fs rise time component, hence our observation of the 1139 cm^{-1} PB* mode appearance. And the later stage of charge transfer that is mainly associated with the photoacidity of HPTS is probed by the increase of the 1334 cm^{-1} band (see Figures 4 and S7), which connects with the blueshifted C–O stretching motion. At this stage, the proton transfers further away from HPTS, and the negative charge residing on the phenolic hydroxyl oxygen atom is no longer stable and needs to shift toward the conjugated ring system, hence the enhancement of the 1334 cm^{-1} band with the fitted rise time constants of ~ 430 fs (55%) and ~ 11 ps (45%). This indicates that charge transfer away from a highly negatively charged oxygen atom in the HPTS anion is much more prominent than that from an oxygen in a neutral hydroxyl group,^{42,49} and the $n\text{--}\pi^*$ charge transfer occurrence has a delayed onset compared with the fastest and dominant phase of ESPT to the acceptor.

Spectral oscillations appear as “quantum beats” in the coherent wavepacket dynamics when various modes are intercorrelated through mechanical coupling or electrostatic interaction, to dissipate excitation energy and guide reaction pathways.^{50–53} A previous report⁷ on the frequency and intensity oscillations of the high-frequency modes of photoexcited wtGFP due to a 120 cm^{-1} two-ring wagging mode demonstrated the crucial role played by that skeletal motion in ESPT confined within the protein pocket. The reaction coordinate of photoexcited HPTS discussed here represents a relevant case for intermolecular ESPT, but due to the abundant presence of individual flexible acceptors (i.e., water, acetate ions) nearby, the reaction pathway is multiplex and more phase space can be accessed on the subpicosecond time scale compared with the well-defined ESPT chain within wtGFP. Quantum effects are expected to play an essential role in sampling solvent configurational space to efficiently transfer the proton from the photoacid molecule to the base, and several characteristic skeletal motions of the HPTS ring system unraveled in this work are certainly prominent coordinates for the initial phase of ESPT reaction. We have also observed a ~ 150 cm^{-1} mode that is plotted in Figure 7. The detailed peak frequency and intensity plot up to 1 ps (Figure S9) suggests the presence of quantum beats with a period of ~ 260 fs, corresponding to a ~ 130 cm^{-1} mode that is likely an in-plane ring rocking mode, which modulates the intermolecular distance between the hydroxyl proton and the bound acceptor (Table 1). Interestingly, the calculation on the HPTS \cdots H₂O

complex shows an intermolecular O(H) \cdots O(H₂) stretching mode at ~ 150 cm^{-1} (0.96 scaling). Plot of the 1139, 930, and 864 cm^{-1} mode frequencies versus time delay (data not shown) displays similar oscillatory patterns with a ~ 260 fs period. Further SNR improvement in this region will render finer details on the highly anharmonic PES where the impulsively excited skeletal motions guide the coherent wavepacket through reduced ESPT barrier to efficiently transfer the proton. The proton transfer will go through a highly inhomogeneous H-bonding network that is constantly rearranging its heavy atom positions on the picosecond time scale.

The comparison between the current data and the 11 mM HPTS in H₂O data (unpublished) provides valuable information. The acetate and acetic acid peaks are both absent in the pure water case, where the 1139 cm^{-1} peak only begins to appear after ~ 2 ps. This shows that water is a less effective proton acceptor in comparison with acetate ion, and one or more water molecules need to get involved to establish the effective H-bonding chain for ESPT. The weak low-frequency modes in S₀ also exhibit increased activity following photoexcitation in pure water, but the ~ 195 cm^{-1} mode has much less intensity and decays much faster than that in 2 M acetate water solution. It indicates that the local field effect⁵⁴ is influencing the activity of specific low-frequency modes, as the observed 195 cm^{-1} mode might be primarily associated with HPTS ring structure having preformed short H-bonds, e.g., HPTS–O \cdots H⁺ \cdots –OOCCH₃ with no intervening water molecules. The relative rigidity of this type of short H-bonds promotes increased activity of this in-plane ring deformation mode to effectively transfer the proton to the already loosely bound acceptor on the subpicosecond time scale.

The ensemble average measurement of excited state structural dynamics through analyzing the aforementioned time-resolved FSRS data is effectively averaging out the stochastic fluctuations of the system, and manifesting the functional molecular motions that are active on the femto-second to picosecond time scale guiding ESPT from PA* to PB*. The intrinsically weak stimulated Raman signal of HPTS, even in the absence of resonance Raman enhancement due to the inflexibility of our Raman pump at ~ 800 nm, can be detected and analyzed through longer acquisition time, higher sample concentration, tighter focusing geometry, higher excitation power, and so forth. We are currently setting up a tunable Raman pump^{55–57} to extend the picosecond pulse wavelength range from 480–720 nm. That way we can tune the versatile Raman pump to the maximum of the transient absorption peak of PA* or PB* to significantly enhance the specific excited state peaks, and obtain further information regarding the intricate yet elegant ESPT process following photoexcitation of HPTS in aqueous solution.

V. CONCLUSIONS

In summary, pyranine (HPTS) has been studied using the newly developed FSRS technique and serves as a pragmatic system to capture the vivid structural snapshots of a reacting molecule undergoing ESPT in aqueous solution. It has been long thought that the proton transfer reaction is a one-dimensional process that simply concerns the proton motion between the donor and acceptor. However, with the advancement of laser technology and emerging techniques such as FSRS, we can finally dissect the PES and capture molecular snapshots as molecules undergo chemical transformation. Ground state FSRS spectra with DFT calculations lay the

solid foundation for Raman peak assignment with the reactant (PA) and product (PB) spectral features attributed to characteristic atomistic motions. Several key low-frequency modes that have not been explicitly observed before are clearly identified in this work particularly in the S_1 state following FC excitation, and their individual functional roles in facilitating intermolecular ESPT through various-length HPTS-water-acetate H-bonding chains are discussed. The subpicosecond germination process of monomer acetic acid and the partially deprotonated HPTS (PB*) with a delayed onset supports the low-frequency mode kinetic analysis, and manifests the prominent intermode correlation in the due course of ESPT on the distinctive time scales of ~ 300 fs, 1 ps, and 90 ps.

These impulsively and coherently excited skeletal modes are highly anharmonic in nature and easily activated by photo-excitation,^{7,22,51,52} evidenced by the strong quantum beats observed for the 150 cm^{-1} mode within 1 ps, and they play an essential functional role in ESPT along other high-frequency coordinates by guiding the wavepacket out of the FC region efficiently toward a reduced-barrier proton transfer pathway on the S_1 PES. The sequential nature of a number of low-frequency modes with pronounced activity on the subpicosecond time scale is unexpected, as the most transient 195 cm^{-1} mode appears the earliest and has the fastest rise time among all the low-frequency modes, whereas the 106 and 321 cm^{-1} modes rise slower and persist longer. The calculations show that these strongly activated low-frequency modes possess the right atomic displacements to facilitate ESPT to nearby acceptors through different vibrational motions. This observation not only confirms the complexity of a seemingly straightforward HPTS–water–acetate system and the multidimensional reaction coordinate for ESPT, but also distinguishes two types of low-frequency modes that are predominantly active in different stages of ESPT with different H-bonding configurations. It is expected that a detailed analysis of these functional low-frequency modes in other similarly prepared systems but with one varying condition, e.g., the acetate concentration, deuteration, or the acceptor strength, will yield further insights into the anharmonicity matrix of multidimensional ESPT in aqueous solution.

■ ASSOCIATED CONTENT

■ Supporting Information

Further discussions on the ground state and excited state FSRS spectra of HPTS in various solutions, peak assignment of acetate and acetic acid in water, steady state spectroscopy using continuous LED illumination at different wavelengths, and additional Figures S1–S9. This information is available free of charge via the Internet at <http://pubs.acs.org>.

■ AUTHOR INFORMATION

Corresponding Author

*E-mail: Chong.Fang@oregonstate.edu.

Notes

The authors declare no competing financial interest.

■ ACKNOWLEDGMENTS

We thank Prof. Joseph Nibler for use of the high-resolution cw Raman setup. We also thank Adam Perry and Liangdong Zhu for help with sample preparation and UV/Vis measurement. This work was supported by the OSU startup research fund and the COS venture fund award to C.F.

■ REFERENCES

- (1) Hynes, J. T. *Nature* **1999**, 397, 565–567.
- (2) Douhal, A.; Lahmani, F.; Zewail, A. H. *Chem. Phys.* **1996**, 207, 477–498.
- (3) Wang, J. H. *Proc. Natl. Acad. Sci. U.S.A.* **1970**, 66, 874–881.
- (4) Kühlbrandt, W. *Nature* **2000**, 406, 569–570.
- (5) Chattoraj, M.; King, B. A.; Bublitz, G. U.; Boxer, S. G. *Proc. Natl. Acad. Sci. U.S.A.* **1996**, 93, 8362–8367.
- (6) Zimmer, M. *Chem. Rev.* **2002**, 102, 759–781.
- (7) Fang, C.; Frontiera, R. R.; Tran, R.; Mathies, R. A. *Nature* **2009**, 462, 200–204.
- (8) Mathies, R. A. *J. Chem. Sci.* **1990**, 103, 283–293.
- (9) Balashov, S. P.; Imasheva, E. S.; Boichenko, V. A.; Antón, J.; Wang, J. M.; Lanyi, J. K. *Science* **2005**, 309, 2061–2064.
- (10) Mondal, S. K.; Sahu, K.; Ghosh, S.; Sen, P.; Bhattacharyya, K. J. *Phys. Chem. A* **2006**, 110, 13646–13652.
- (11) Genosar, L.; Cohen, B.; Huppert, D. J. *Phys. Chem. A* **2000**, 104, 6689–6698.
- (12) Tran-Thi, T.-H.; Gustavsson, T.; Prayer, C.; Pommeret, S.; Hynes, J. T. *Chem. Phys. Lett.* **2000**, 329, 421–430.
- (13) Spry, D. B.; Goun, A.; Fayer, M. D. *J. Phys. Chem. A* **2007**, 111, 230–237.
- (14) Nibbering, E. T. J.; Fidler, H.; Pines, E. *Annu. Rev. Phys. Chem.* **2005**, 56, 337–367.
- (15) Rini, M.; Magnes, B.-Z.; Pines, E.; Nibbering, E. T. J. *Science* **2003**, 301, 349–352.
- (16) Mohammed, O. F.; Dreyer, J.; magnes, B.-Z.; Pines, E.; Nibbering, E. T. J. *ChemPhysChem* **2005**, 6, 625–636.
- (17) Mohammed, O. F.; Pines, D.; Dreyer, J.; Pines, E.; Nibbering, E. T. J. *Science* **2005**, 310, 83–86.
- (18) Siwick, B. J.; Bakker, H. J. *J. Am. Chem. Soc.* **2007**, 129, 13412–13420.
- (19) Cox, M. J.; Bakker, H. J. *J. Chem. Phys.* **2008**, 128, 174501.
- (20) Peteanu, L. A.; Mathies, R. A. *J. Phys. Chem.* **1992**, 96, 6910–6916.
- (21) Chudoba, C.; Riedle, E.; Pfeiffer, M.; Elsaesser, T. *Chem. Phys. Lett.* **1996**, 263, 622–628.
- (22) Pfeiffer, M.; Lau, A.; Lenz, K.; Elsaesser, T. *Chem. Phys. Lett.* **1997**, 268, 258–264.
- (23) Lochbrunner, S.; Wurzer, A. J.; Riedle, E. J. *Chem. Phys.* **2000**, 112, 10699–10702.
- (24) Lochbrunner, S.; Stock, K.; Riedle, E. J. *Mol. Struct.* **2004**, 700, 13–18.
- (25) Lochbrunner, S.; Szeghalmi, A.; Stock, K.; Schmitt, M. J. *Chem. Phys.* **2005**, 122, 244315.
- (26) Coe, J. D.; Levine, B. G.; Martínez, T. J. *J. Phys. Chem. A* **2007**, 111, 11302–11310.
- (27) Levine, B. G.; Martínez, T. J. *Annu. Rev. Phys. Chem.* **2007**, 58, 613–634.
- (28) Brejc, K.; Sixma, T. K.; Kitts, P. A.; Kain, S. R.; Tsien, R. Y.; Ormo, M.; Remington, S. J. *Proc. Natl. Acad. Sci. U.S.A.* **1997**, 94, 2306–2311.
- (29) Mandal, D.; Tahara, T.; Meech, S. R. *J. Phys. Chem. B* **2004**, 108, 1102–1108.
- (30) Stoner-Ma, D.; Jaye, A. A.; Ronayne, K. L.; Nappa, J.; Meech, S. R.; Tonge, P. J. *J. Am. Chem. Soc.* **2008**, 130, 1227–1235.
- (31) Meech, S. R. *Chem. Soc. Rev.* **2009**, 38, 2922–2934.
- (32) Martinez, T. J. *Nature* **2010**, 467, 412–413.
- (33) McCamant, D. W.; Kukura, P.; Yoon, S.; Mathies, R. A. *Rev. Sci. Instrum.* **2004**, 75, 4971–4980.
- (34) Kukura, P.; McCamant, D. W.; Mathies, R. A. *Annu. Rev. Phys. Chem.* **2007**, 58, 461–488.
- (35) Frontiera, R. R.; Fang, C.; Dasgupta, J.; Mathies, R. A. *Phys. Chem. Chem. Phys.* **2012**, 14, 405–414.
- (36) Kukura, P.; McCamant, D. W.; Yoon, S.; Wandschneider, D. B.; Mathies, R. A. *Science* **2005**, 310, 1006–1009.
- (37) McCamant, D. W.; Kukura, P.; Mathies, R. A. *J. Phys. Chem. B* **2005**, 109, 10449–10457.

- (38) Dasgupta, J.; Frontiera, R. R.; Taylor, K. C.; Lagarias, J. C.; Mathies, R. A. *Proc. Natl. Acad. Sci. U.S.A.* **2009**, *106*, 1784–1789.
- (39) Frontiera, R. R.; Dasgupta, J.; Mathies, R. A. *J. Am. Chem. Soc.* **2009**, *131*, 15630–15632.
- (40) Shim, S.; Dasgupta, J.; Mathies, R. A. *J. Am. Chem. Soc.* **2009**, *131*, 7592–7597.
- (41) Frisch, M. J.; Trucks, G. W.; Schlegel, H. B.; Scuseria, G. E.; Robb, M. A.; Cheeseman, J. R.; Scalmani, G.; Barone, V.; Mennucci, B.; Petersson, G. A.; Nakatsuji, H.; Caricato, M.; Li, X.; Hratchian, H. P.; Izmaylov, A. F.; Bloino, J.; Zheng, G.; Sonnenberg, J. L.; Hada, M.; Ehara, M.; Toyota, K.; Fukuda, R.; Hasegawa, J.; Ishida, M.; Nakajima, T.; Honda, Y.; Kitao, O.; Nakai, H.; Vreven, T.; J. A. Montgomery, J.; Peralta, J. E.; Ogliaro, F.; Bearpark, M.; Heyd, J. J.; Brothers, E.; Kudin, K. N.; Staroverov, V. N.; Kobayashi, R.; Normand, J.; Raghavachari, K.; Rendell, A.; Burant, J. C.; Iyengar, S. S.; Tomasi, J.; Cossi, M.; Rega, N.; Millam, J. M.; Klene, M.; Knox, J. E.; Cross, J. B.; Bakken, V.; Adamo, C.; Jaramillo, J.; Gomperts, R.; Stratmann, R. E.; Yazyev, O.; Austin, A. J.; Cammi, R.; Pomelli, C.; Ochterski, J. W.; Martin, R. L.; Morokuma, K.; Zakrzewski, V. G.; Voth, G. A.; Salvador, P.; Dannenberg, J. J.; Dapprich, S.; Daniels, A. D.; Farkas, Ö.; Foresman, J. B.; Ortiz, J. V.; Cioslowski, J.; Fox, D. J. *Gaussian 09*, revision B.1; Gaussian, Inc.: Wallingford, CT, 2009.
- (42) Granucci, G.; Hynes, J. T.; Millie, P.; Tran-Thi, T.-H. *J. Am. Chem. Soc.* **2000**, *122*, 12243–12253.
- (43) Gauffrès, R.; Maillols, J.; Tabacik, V. *J. Raman Spectrosc.* **1981**, *11*, 442–448.
- (44) Bertie, J. E.; Michaelian, K. H. *J. Chem. Phys.* **1982**, *77*, 5267–5271.
- (45) Olbert-Majkut, A.; Ahokas, J.; Lundell, J.; Pettersson, M. *J. Raman Spectrosc.* **2011**, *42*, 1670–1681.
- (46) Agmon, N. *Chem. Phys. Lett.* **1995**, *244*, 456–462.
- (47) Meiboom, S. *J. Chem. Phys.* **1961**, *34*, 375–388.
- (48) Montrose, C. J.; Bucaro, J. A.; Marshall-Coakley, J.; Litovitz, T. *J. Chem. Phys.* **1974**, *60*, 5025–5029.
- (49) Hynes, J. T.; Tran-Thi, T.-H.; Granucci, G. *J. Photochem. Photobiol. A Chem.* **2002**, *154*, 3–11.
- (50) Engel, G. S.; Calhoun, T. R.; Read, E. L.; Ahn, T.-K.; Mancal, T.; Cheng, Y.-C.; Blankenship, R. E.; Fleming, G. R. *Nature* **2007**, *446*, 782–786.
- (51) Wang, Q.; Schoenlein, R. W.; Peteanu, L. A.; Mathies, R. A.; Shank, C. V. *Science* **1994**, *266*, 422–424.
- (52) Zhu, L.; Sage, J. T.; Champion, P. M. *Science* **1994**, *266*, 629–632.
- (53) Collini, E.; Wong, C. Y.; Wilk, K. E.; Curmi, P. M. G.; Brumer, P.; Scholes, G. D. *Nature* **2010**, *463*, 644–647.
- (54) McHale, J. L. *Molecular Spectroscopy*; Prentice-Hall: Upper Saddle River, NJ, 1999.
- (55) Shim, S.; Mathies, R. A. *Appl. Phys. Lett.* **2006**, *89*, 121124.
- (56) Kovalenko, S. A.; Dobryakov, A. L.; Ernsting, N. P. *Rev. Sci. Instrum.* **2011**, *82*, 063102.
- (57) Pontecorvo, E.; Kapetanaki, S. M.; Badioli, M.; Brida, D.; Marangoni, M.; Cerullo, G.; Scopigno, T. *Opt. Express* **2011**, *19*, 1107–1112.